Spatio-temporal evolution of long-range transported mineral desert dust properties over rural and urban sites in Central Europe

Dominika M. Szczepanik [a], Patryk Poczta [b], Camelia Talianu [c,d], Christine Böckmann [e,f], Christoph Ritter [e], Horatiu Stefanie [a,g], Florica Toanca [c], Bogdan H. Chojnicki [b], Dirk Schüttemeyer [h], Iwona S. Stachlewska [a,*]

[a] University of Warsaw, Faculty of Physics, Pasteura 5, 02-093 Warsaw, Poland
[b] Poznan University of Life Sciences, Faculty of Environmental and Mechanical Engineering, Piatkowska 94, 60-649 Poznan, Poland
[c] National Institute of Research and Development for Optoelectronics, Atomistilor 409, RO77125 Măgurele, Romania
[d] University of Natural Resources and Life Sciences, Institute of Meteorology and Climatology, Gregor-Mendel-Straße 33, 1180 Vienna, Austria
[e] Alfred Wegener Institute, Helmholtz Centre for Polar and Marine Research, Telegrafenberg A45, 14473 Potsdam, Germany
[f] University of Potsdam, Institute of Mathematics, Karl-Liebknecht-Str. 24-25, 14476 Potsdam, Germany
[g] Babes-Bolyai University, Faculty of Environmental Science and Engineering, Fantanele Street 30, RO400294 Cluj-Napoca, Romania
[h] European Space Agency, European Space Research and Technology Centre, Keplerlaan 1, 2201 Nordwijk, the Netherlands

HIGHLIGHTS

- Even rapid Saharan mineral dust inflow can be affected by transport pathways.
- Local peatland decreases polarizing properties of transported mineral dust.
- NMMB/BSC-Dust model underrates the extent of mineral dust over Eastern Europe;

GRAPHICAL ABSTRACT
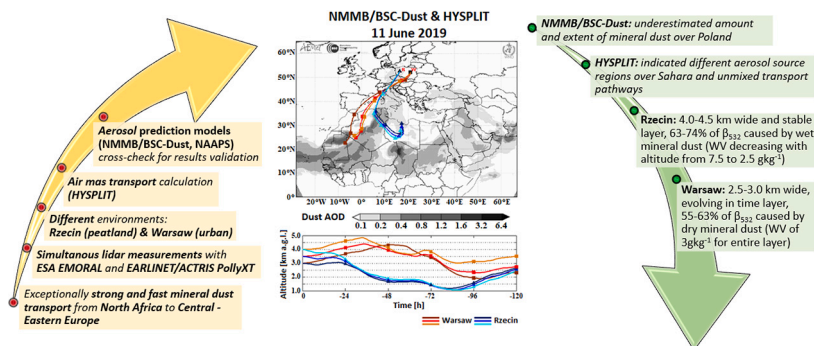
ARTICLE INFO

Editor: Anastasia Paschalidou

ABSTRACT

An exceptionally strong and very fast (120h) mineral dust inflow from North Africa to Poland was predicted by NMMB/BSC-Dust and NAAPS models on 10–11 June 2019. Simultaneous measurements with two complex lidar systems at the EARLINET-ACTRIS urban site in Warsaw (Central Poland) and the PolWET peatland site in Rzecin (Western Poland) captured the evolution of this dust event. The advected air masses had different source areas in North Africa, they were reaching each station via independent pathways, and thus, were unlikely mixed with each other. The excellent capabilities of the next generation PollyXT lidar and the mobile EMORAL lidar allowed for the derivation of full datasets of aerosol optical properties profiles that enabled comparative study of the advected dust properties evolution. Within a mere 350 km distance between Warsaw and Rzecin, distinctly different dust properties were measured, respectively: dry mineral dust composed mainly of coarse mode dust

* Corresponding author.
  E-mail address: iwona.stachlewska@fuw.edu.pl (I.S. Stachlewska).

particles (50 ± 5 % of the total particle backscattering profile) versus the wet mineral dust dominated by fine dust particles (58 ± 4 %). A new parameter fine-to-coarse dust ratio (FCDR) is proposed to describe more intuitively mineral dust composition.

1. Introduction

Airborne mineral dust particles influence climate and environmental conditions due to the direct aerosol effect (e.g. Kok et al., 2017; Di Biagio et al., 2020) and the indirect aerosol-cloud effect (e.g. McCoy et al., 2017). Mineral dust particles are efficient cloud condensation nuclei (Marinou et al., 2019) that lead to changes in the optical properties and lifetime of clouds and influence precipitation (Karydis et al., 2011). Consequently, radiative forcing is influenced (Seinfeld et al., 2016), and therefore, dust-climate feedback is a relevant process to study. To make correct assessments of this phenomenon one needs both a) knowledge of the possible source and pathway of mineral dust, and b) its optical and microphysical properties. In this paper, we try to answer the question of to what extent it is important and worth the effort to study the vertical, horizontal, and temporal variability of long-range transport of aerosol at the same time, at two different places separated within the mesoscale?

The Sahara desert is the main source of mineral dust transported over long-range distances over the entire Europe. Dust observations are frequent over Southern Europe, e.g. Spain (Mandija et al., 2017), Italy (Calidonna et al., 2020), Greece (Marinou et al., 2019), central Europe, e.g. Switzerland (Navas-Guzmán et al., 2019), Poland (Janicka et al., 2017; Szczepanik et al., 2021), Eastern Europe, e.g. Romania (Mărmureanu et al., 2019; Ajtai et al., 2020) or as high north as Norway, e.g. Groot Zwaaftink et al. (2022). Such dust intrusions can be tracked (for finding the origin or destination) with the HYSPLIT (Draxler and Rolph, 2012, Stein et al., 2015) and FLEXPART (Pisso et al., 2019) transport models. Source analysis can be done using a combination of those transport models and the prediction models such us NMMB/BSC-Dust (Pérez et al., 2011), NAAPS (Hogan and Rosmond, 1991). For this, knowledge on the physical and chemical properties of mineral dust is required (Formenti et al., 2011), along with identification of dust sources and appropriate deposition schemes that are crucial for dust-emission models (Feuerstein and Schepanski, 2019) and weather forecast models (Tsarpalis et al., 2018).

For biogeochemistry and climate modelling, different properties of the dust particles must be taken into consideration, i.e. size distribution (Mahowald et al., 2010, 2014), which is mainly described as a ratio of fine and coarse aerosol particles. The dust fine mode particles are composed of particles with sizes below 2.5 μm. The dust coarse mode covers the particle size spectrum with a diameter higher or equal to 2.5 μm (Seinfeld and Pandis, 2006). Several lidar studies showed that coarse and giant particles are ubiquitous in Saharan dust export regions and are radiatively significant over the Sahara (Ryder et al., 2019). Moreover, hygroscopicity in relation to dust is of great importance (Hara et al., 2018; Navas-Guzmán et al., 2019; Wu et al., 2020). Finally, real-time lidar measurements of the dust-cloud interaction (Huang et al., 2018, Wang et al., 2020), especially the impact of mineral dust on cloud formation (Weger et al., 2018) and new particle formation (Miffre et al., 2019) are important.

In this work we want to stress the possibilities of linking the capabilities of automatic complex lidar measurements and retrieval with the use of the Single Calculus Chain, which can lead to the near real-time studies in the future. One of the crucial tasks of the ACTRIS is establishing the optimal distance between stations within the measuring network of existing and to be developed in the future research performing organizations infrastructures. The question is: how should the stations be deployed? Which localizations are the best for conducting relevant studies? What are the footprints of the stations? Is it worth adding new stations? The current paper aims at investigating the lidar-derived optical properties of long-range transported mineral dust with

source areas over different parts over Northern Africa. So far, this has never been studied/reported for East-Central Europe. Additionally, we try to give the answer to this question in the case of additional lidar site in East-Central Europe.

The paper is structured as follows. In Section 2, the measuring sites and instrumentation are described. Section 3 is dedicated to the methodology applied to lidar data analysis and interpretation. Section 4 discusses the obtained optical properties of mineral dust, as well as the separation of mineral dust with the multi-aspect interpretation of the results. In Conclusions (Section 5), the main findings are summarized.

2. Measuring sites and instrumentation

The dust event was observed independently at two sites in Poland operated within the Aerosol Research Network PolandAOD (http://polandaod.pl; last access on 12.05.2023) located in Warsaw agglomeration and over the Rzecin peatland. The sites were equipped with advanced lidar systems regarded as core instruments, measuring simultaneously in an approximate straight-line distance of 350 km. The auxiliary observations were used as well, such as co-located sun-photometer in Warsaw and cloud radar and microwave radiometer in Rzecin. For the interpretation of measurements and derived data products, the air-mass dispersion, aerosol source, composition, and type were provided by the means of the prediction, re-analysis, and transport model runs.

2.1. PollyXT lidar at the Remote Sensing Laboratory in Warsaw

2.1.1. The Remote Sensing Laboratory (RS-Lab)

The Remote Sensing Laboratory (RS-Lab) of the Faculty of Physics, University of Warsaw is situated close to the city centre of Warsaw (52.21 N, 20.98E, 112 m a.s.l.) – the capital of Poland. Warsaw has an area of 517 km^2 with 1,744,000 inhabitants. As for a land use it is characterized by a significant amount of green areas (43 % of the city space) with a comparable area of residential sites (44 %), whole transport and infrastructural areas cover only 13 % of the city (Żmudzka et al., 2019). The city is characterized by a warm temperate climate, with warm summers (mean annual temperature of 18.1–19.1 °C), thermally specific winters (a mean annual temperature from -0.6 to -1.2 °C), and an annual mean precipitation sum of 530–580 mm (the reference period of 1981–2014, Żmudzka et al., 2019). Increasingly, the urban heat island effect is observed (rising number of days with temperatures >30 °C in the city centre measurements; Żmudzka, 2016), sometimes lasting up to several days (the heat waves episodes; Stachlewska et al., 2018).

The RS-Lab station has been operating since July 2013 and is a recognizable measuring site within the ACTRIS-EARLINET and AERO-NET NASA networks (Fig. 1). Among other instrumentation, it is equipped with the PollyXT lidar (core) and CIMEL 318CE sun photometer, operated in an automatic 24/7 mode.

2.1.2. The automated multi-wavelength Raman polarization and water-vapour PollyXT lidar

The automated multi-wavelength Raman polarization and water-vapour PollyXT lidar, comprises of the 20 Hz Nd-YAG laser, emitting three laser beams (1064, 532 and 355 nm). Light pulses are simultaneously and co-axially sent into the atmosphere, after being expanded to a 45 mm diameter to decrease the beam divergence (0.2 mrad) and lower the output power (180/110/60 mJ), respectively. The backward scattered light is collected with a Newtonian reflector of 300 mm
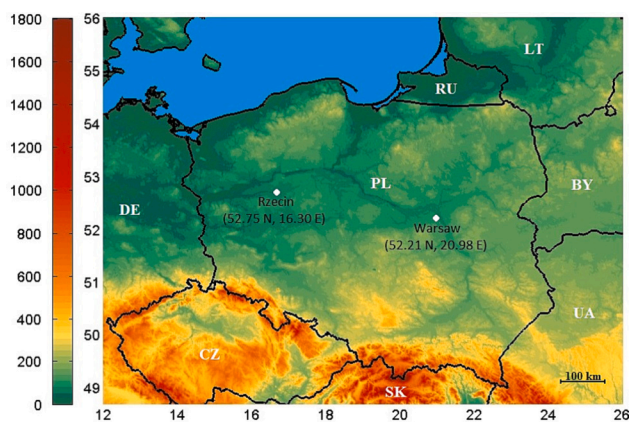
Fig. 1. Hypsometric map of Poland with the location of measuring sites: the rural site over Rzecin peatland, the urban site in agglomeration of Warsaw, capital of Poland (350 km apart); diagram courtesy of Olga Zawadzka-Mańko (FUW).

primary mirror, 0.9 mm pinhole (1 mrad narrow field of view; the PollyXT lidar; Engelmann et al., 2016). It is used to determine the elastic scattering at 1064, 532, and 355 nm, the elastic cross-polarized scattering at 532 and 355 nm, the vibrational Raman scattering for N_2 at 607 and 387 nm and for H_2O at 407 nm. The vertical profiles of three particle backscattering coefficients (β), two particle extinction coefficients (α), two particle and volume linear depolarization ratios (δ_p and δ_v), and a water vapour mixing ratio (WV), are provided (so-called sets of $3\beta + 2\alpha + 2\delta + WV$). For all channels, solely photon-counting detection is done with the Hamamatsu H10721P-110 photomultipliers (dead time of ~2 ns), except for the 1064 nm wavelength where the extra-cooled Hamamatsu R3236 is used. The signals are acquired with 600 MHz photon counters (providing 7.5 m height and 30 s time resolutions) and are recorded up to 48 km with 250 range bins pre-trigger length. For all detection channels, narrow-bandwidth interference filters of 1 nm and 0.3 nm (N_2 Raman channels) are used to achieve at least 8 times suppression.

2.2. EMORAL lidar at the PolWet PULS site in Rzecin peatland

The PolWET station of the Poznan University of Life Sciences in Rzecin (52.76 N, 16.31 E, 56 m a.s.l., Fig. 1) is located over a large peatland area in the Puszcza Notecka forest (Western Poland), which is protected within the Natura 2000 Network (PLH300019) under the Habitats Directive (Harenda et al., 2021). The peatland is classified as fen with three main phytocoenosis (Chojnicki et al., 2007). The southern part is dominated by *Carex* spp., and the northern part by *Phragmites australis* (Cav.) *Trin. Ex Steud* and *Sphagnum* spp. The central part of the peatland with a 70 cm thick floating peat carpet is more biodiverse, covered by *Carex rostrata* L., *Carex limosa* L., *Oxycoccus palustris* L., *Typha latifolia* L., *Typha angustifolia* L. and *Sphangum* spp. The drought periods of past years have caused the appearance of pine trees and bushes on the surface of the peatland. The site climate is typical for Central Europe and it is the result of both oceanic (more often) and continental air masses, with the mean annual air temperature in the Rzecin region of 8.63 °C (the reference period of 1981–2010), with January and July means of −0.93 °C and 18.88 °C, respectively (IMGW-PIB, 2021). The average annual precipitation is 551 ± 25 mm (Woś, 2010), with the highest precipitation in July.

Standard operation at PolWET station contains measurements of CO_2/H_2O fluxes exchange between the ecosystem and the atmosphere (using eddy covariance technique), as well as a set of meteorological parameters: air and soil temperature, relative humidity, precipitation, shortwave radiation (total, diffused and reflected), longwave radiation, photosynthetic photon flux density, and water table depth (Harenda

et al., 2021). These data were not used in our study. However, within POLIMOS activity an extensive field campaign was conducted in June––August 2019 in Rzecin. A unique set of instruments was deployed: the EMORAL lidar (core), the BASTA cloud radar provided by LATMOS and the Microwave radiometer MWR provided by INOE. Cloud radar and radiometer data were used in this work as auxiliary information.

2.2.1. The ESA Mobile Raman Lidar (EMORAL)

The ESA Mobile Raman Lidar (EMORAL) was installed at the Rzecin peatland in 2018–2019 in the framework of the POLIMOS activity. The lidar is installed in a van. This allows for taking the measurements in a chosen place where it is possible to drive. In the case of this campaign, no observations while driving were taken. The van was located on the dedicated platform at the measuring site, since the peatland is a protected area. It comprises an Nd:YAG laser head, the 300 mm diameter Cassegrain telescope with an adjustable field of view of 2–3.6 mrad, and fast high-resolution transient recorders (TR40–160, 16 bits, Licel GmbH, Germany). The laser beams are emitted simultaneously, collinearly, and vertically with a pulse length of 5–7 ns and repetition rate of 10 Hz at three wavelengths 1064/532/355 nm with a pulse energy of 112/103/ 128 mJ respectively. Collected backward scattered radiation is detected at 8 channels: 3 elastic (1064/532/355 nm), 3 vibrational Raman (607/ 387 nm for N_2 molecules and 408 nm for H_2O particles) and 2 depolarizing channels (532/355 nm) and simultaneously recorded with an analog and photon-counting mode – except for 1064 nm (only analog). Lidar is providing the sets of $3\beta + 2\alpha + 2\delta + WV$. Raw spatial resolution is 3.75 m and the height of the full overlap is about 300 m a.g.l. Data acquisition for the studied days was set up at 30 s.

Both lidars are fulfilling the strict requirements of the Quality Assurance (QA) instrumental procedures of ACTRIS-EARLINET (Freudenthaler et al., 2018). Lidar raw data files and the lidar-derived high-quality profiles are stored and are publicly available via the PolandAOD Archive. The Warsaw data are also stored in the ACTRIS-EARLINET Data Base after passing Quality Control (QC) procedures (Amato et al., 2018). More details about requirements that are fulfilled can be found at the European Aerosol Research Lidar NETwork EARLINET website (http: //www.earlinet.org/, last access 20.04.2023).

3. Data analysis and interpretation methodology

The methodology for lidar data evaluation comprised of several steps depicted in the work-flow diagram in Fig. 2, i.e. selection of the mineral dust case study, calculation of the sets of optical and microphysical properties, estimation of the fine and coarse mode dust contributions, interpretation of the results with model data in terms of aerosol source.

3.1. Optical properties retrieval from lidar data

The data collected with PollyXT lidar in Warsaw (photoncounting signals, 30 s and 7.5 m resolution), were evaluated to obtain the vertical profiles of the aerosol optical properties using automated procedures implemented in the Single Calculus Chain (SCC, version 5.2.3; D'Amico et al., 2015). The SCC is an automated tool, recommended by EARLINET/ACTRIS, for lidar data evaluation, available online to any user via the password-protected user account (D'Amico et al., 2016, https ://scc.imaa.cnr.it/, last access 12.07.2023). It allows for data retrieval using a method selected by the user (e.g., Klett, Raman, polarization calibration). Additionally, all data products have user-selected properties (e.g., calibration values and range, error calculation method and thresholds, altitude range of the profile). The evaluation process is automatic and connected to a specified lidar configuration, consisting of both emission and detection system properties. The raw PollyXT signals were processed with the raw vertical resolution for integration time in the range of 45–60 min and error threshold of 50 % and 50–100 % for altitudes <2 km and > 2 km, respectively (D'Amico et al., 2016). The particle backscatter coefficients (β) at 355, 532 and 1064 nm, the
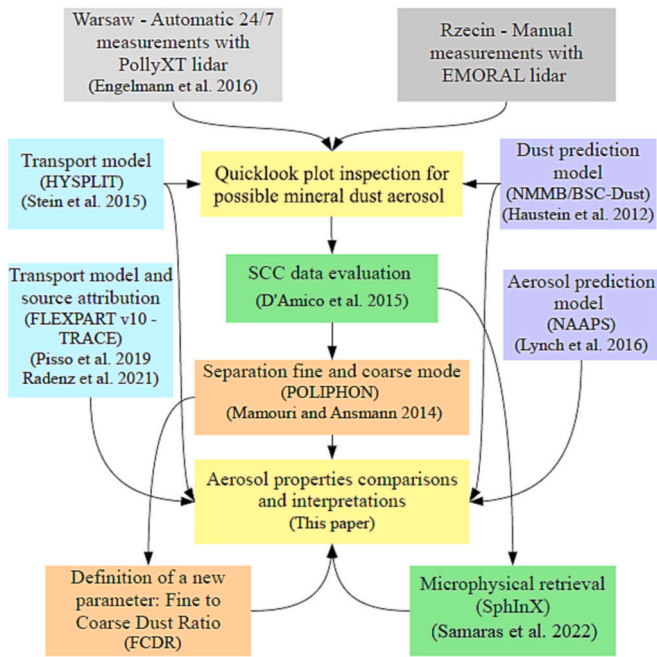
Fig. 2. Methodology work-flow diagram applied for analysis at both measuring sites.

particle extinction coefficients (α) at 355 and 532 nm, and the particle linear depolarization ratios (δ_p) at 532 nm were evaluated using the Raman method (for day and night-time) by means of the so-called *Raman Backscatter, Lidar ratio and extinction,* and *Raman backscatter and linear depolarization ratio* SCC data products (Mattis et al., 2016). Note that in case of Warsaw, only the δ_p at 532 nm is being discussed since cross-polarization channel at 355 nm was not working in July 2019. The calibration of backscatter coefficients was done with the atmospheric profiles of the rawinsonde RS92 (Vaisala) launched at the World Meteorological Organization station WMO 12374 in Legionowo (52.40 N, 20.96 E, 96 m a.s.l, 25 km north of Warsaw. A value of a backscattering ratio of 1.00 for all wavelengths was used. The calibration Angstrom Exponent value for the extinction coefficient profiles calculation was set to 1 (Ansmann et al., 1990). For the night-time measurements the water vapour mixing ratio (WV) was obtained manually, as the ratio of the Raman H_2O and N_2 channels, using method described in Stachlewska et al., 2017. The linear polarization calibration was done using the $\pm45°$ method applied on automated calibration measurements conducted twice a day (each lasting 10 min, starting at 2:30 UTC and 17:30 UTC) as in Engelmann et al. (2016).

The data from EMORAL lidar in Rzecin (analog and photoncounting signals, 30s and 3.75 m resolution) were also evaluated using SCC procedures (SCC version 5.1.4; D'Amico et al., 2015). The profiles presented in this work were obtained from signals detected only in analogue mode, with the raw vertical resolution for integration time in the range of 14–60 min and with an error threshold of 5 % and 10–30 % for altitude <2 km and > 2 km respectively (D'Amico et al., 2016). The β, α and δ_p profiles were calculated at the same wavelengths as for PollyXT, using the Raman method (at day and night-time) with SCC products as for PollyXT (Mattis et al., 2016). The exception was the molecular contribution of the β profiles that was done using a standard atmosphere model profiles and a backscatter ratio of 1.03 for 355 and 1.05 for 532 and 1064 nm. The Angstrom Exponent for α profiles calculation was also 1 (Ansmann et al., 1990). The δ_p profiles were calibrated using the $\pm45°$ method (in manual mode) as in Engelmann et al. (2016). The WV profiles were obtained using the method by Stachlewska et al., 2017.

More detailed information about SCC products is provided in Appendix A, Table A1.

3.2. Separation of fine and coarse dust

The extended POlarization-LIdar PHOtometer Networking (POLIPHON) method (Mamouri and Ansmann, 2014) was applied for the separation of dust (fine and coarse mode) and non-dust particles contribution to the backscattering coefficient. Szczepanik et al., 2021, showed that application of this code is feasible for Warsaw, thus in the current work the separation algorithm was applied with high confidence on both sites. For easier interpretation of the results in a comparative approach, we introduce here a new parameter, called Fine to Coarse Dust Ratio (FCDR), which is defined as follows:

$$FCDR = \frac{\beta_{df}}{\beta_{df} + \beta_{dc}}, \tag{1}$$

where β_{df} and β_{dc} denotes the backscatter coefficient on fine and coarse dust particles, respectively. The values of this parameter is of the range $(0; 1]$. Values close to 0 are corresponding to the coarse dust dominance, while 1 stays for the fine dust only. The values in between correspond to the mineral dust fractions mixtures, whereby fractions are the same when the FCDR is equal to 0.5. Note that this is not the Fine Mode Fraction 500 nm given by the AERONET.

3.3. Microphysical parameters inversion from lidar data

3.3.1. The spheroidal inversion experiments (SphInX)

The spheroidal inversion experiments (SphInX) model has been developed at the University of Potsdam (Böckmann and Osterloh, 2014; Samaras, 2016; Samaras et al., 2022). A SphInX software tool was created to handle non-spherical particles using a two-dimensional extended Mie model and considering non-spherical, e.g. mineral dust particles, with a spheroidal-particle approximation.

Such non-spherical approximation was also used, e.g., by (Veselovskii et al., 2016; Dubovik et al., 2006; Soupiona et al., 2019). Denoting the semi-minor axis of the rotating ellipse with c and the semi-major axis with b, the aspect ratio (a = c/b) gives three particle shapes: oblate, sphere, and prolate. After retrieving the two-dimensional volume size distribution one can calculate the following microphysical parameters:

the total volume concentration: $v_t = \int_{a_{min}}^{a_{max}} \int_{r_{min}}^{r_{max}} v(r,a)drda$,

the total surface-area concentration: $a_t = \int_{a_{min}}^{a_{max}} \int_{r_{min}}^{r_{max}} \frac{3}{\pi r^3} G(r,a)v(r,a)drda$,

the effective radius $r_{eff} = 3\frac{v_t}{a_t}$, and

the effective aspect ratio $a_{eff} = \frac{\int_{a_{min}}^{a_{max}} a \int_{r_{min}}^{r_{max}} v(r,a)drda}{v_t}$.

The function $G(r,a)$ denotes the spheroidal geometrical cross section of the particle, which can be computed by:

$$G(r,a) = \begin{cases} 2\pi\left[c^2 + \frac{b^2}{e}tanh^{-1}(e)\right], & \text{where } e = \sqrt{1 - \frac{b^2}{c^2}}, & \text{if } a < 1 \\ 4\pi r^2, & & \text{if } a = 1 \\ 2\pi\left[c^2 + \frac{cb}{e}sinh^{-1}e\right], & \text{where } e = \sqrt{1 - \frac{c^2}{b^2}}, & \text{if } a > 1 \end{cases} \tag{2}$$

Note that r plays the role of a radius of a fictitious spherical particle with equal volume to the actual spheroidal one. SphInX operates with expendable pre-calculated discretization databases based on a spline collocation and on look-up tables of scattering efficiencies using T-matrix theory (Rother and Kahnert, 2009). Concerning the available regularization methods and the parameter choice rules that the algorithm requires to use for the ill-posed model, a selection of the following is possible, see e.g. Hansen (2010) for the first four and Böckmann and Kirsche (2006) and Böckmann and Osterloh (2014) for last two:

i. Truncated singular value decomposition (TSVD) with the discrepancy principle (DP),
ii. Tikhonov regularization with the L-curve method (LC),
iii. Tikhonov regularization with the generalized cross validation method (GCV),
iv. Tikhonov regularization with DP,
v. Padé iteration (Generalized Runge–Kutta Regularizers) with LC, and
vi. Padé iteration with DP or fixed iteration number, e.g. empirical value 30.

The spheroidal scattering efficiencies depend on the complex refractive index (CRI). SphInX is using a CRI grid, which should be given in separate real and imaginary parts. Ideally, this grid can be further confined if there is sufficient knowledge on aerosol composition (or the exact CRI).

The optical data profiles obtained from averaged vertical profiles of the aerosol optical properties of Raman lidar observations should be available at least for 3 backscatter, 2 extinction coefficients and 2 particle linear depolarization ratios since the model is ill-posed as well as limited to dust fine mode particles below 2.2 μm. In case of the non-spherical model the contributions from the cross and parallel back-scattering channels to a total backscatter is needed. This is here only fulfilled for case Rzecin especially for G2 group. To achieve the mentioned contributions there was a need of manual data evaluation for this special case. Next, a homogeneous layer of interest (here two layers 2.0–2.4 km and 3.0–3.725 km) has to be selected where the LR and AE values are constant or quite constant showing homogeneity inside the plume. The microphysical parameters given below are the mean values of the methods (ii), (v) and (vi) with standard deviation.

3.4. Models used for data interpretation

3.4.1. The Hybrid Single Particle Lagrangian Integrated Trajectory model (HYSPLIT)

The Hybrid Single Particle Lagrangian Integrated Trajectory model (HYSPLIT) is a numeric model for air-mass movement trajectories dedicated to reconstructing their origins. It is a commonly used model for the estimation of transport and dispersion of aerosol. The calculation method is a mixture of the Lagrangian and Eulerian approaches, described in detail by Stein et al., 2015. In this study, the HYSPLIT model was used with the reanalysis meteorological data (Reanalysis 1 Jun 2019, CDC1 Meteorological Data). Calculated backward trajectories of the air-masses movement were used to assess the possible type of aerosol, based on its source. Trajectories were calculated mainly in the free troposphere at the altitudes within the observed aerosol plume (at 3.5, 4.0, and 4.5 km), lasting 120 h. Backward trajectories were calculated for every 6 h starting from 12:00 UTC on 10.06.2019 and ending at 12:00 UTC on 11.06.2019. Additional trajectories were calculated at 18:00 UTC and 22:00 UTC on 10.06.2019, which are selected periods for comparison in observations provided from two measuring sites; for brevity, not shown.

3.4.2. The Flexible Particle Dispersion model (FLEXPART)

The Flexible Particle Dispersion model (FLEXPART) is a particle dispersion model designed to compute long-range transport, taking into account the diffusion, the dry and the wet deposition of particles. FLEXPART produces an output suitable for inverse determination of emission aerosol sources, e.g. of greenhouse gases, dust or volcanic ash. The model ingests ECMWF (European Centre for Medium Range Weather Forecasts) and GFS (Global Forecast System) 3-D meteorological fields and solves the equations for transport, turbulent diffusions, and other relevant processes in a Lagrangian framework (Stohl et al., 2005). FLEXPART can be run in forward and backward modes. In forward mode, it simulates the transport and dispersion of emissions from given sources towards receptor points, producing gridded output concentration and deposition. In backward mode, it produces the source-receptor relationship with respect to a point source or gridded sources for given receptors (Seibert and Frank, 2004). The FLEXPART use the plume of the trajectories, which is the centroid of the trajectories clusters (all possible trajectories using the input conditions). So, basically this is the uncertainty assessment of the trajectory. Also the meteorological input parameters do not have uncertainties, the ERA 5 provides only the average values (wind field average). The difference between the models is that FLEXPART uses a Lagrangian particle approach, while HYSPLIT uses a hybrid approach that combines Lagrangian and Eulerian methods. The relative error computed as distance between points of FLEXPART trajectory and HYSPLIT trajectory was lower than 10 %. For our study, we do not identify a precise location of the dust source, but a large source (e.g. Sahara desert).

For this study, the FLEXPART version 10 was used (Pisso et al., 2019). The meteorological data used as input are obtained from the ECMWF global meteorological fields with a horizontal resolution of 1.0 × 1.0, a temporal resolution of 3 h, using the lowest 70 vertical levels (corresponding to pressure levels from surface to 150 hPa) out of the 137 vertical levels. The transport of aerosols for each lidar station is simulated taking into account all atmospheric processes (clouds, wet and dry deposition, aging, etc.) starting with 10,000 particles tracked backward for 5 days (120 h), with the particle positions being stored every hour. These simulations are run every hour for the whole period of interest. The model output is gridded to height steps of 500 m, starting from the ground up to 10 km.

To classify the potential source regions of the long-range transported mineral dust, an automated time-height-resolved air mass source attribution software (TRACE), based on FLEXPART, was used (Radenz et al., 2021). TRACE uses two methods to classify the regions with potential sources of aerosols. The first method, based on a simplified version of the MODIS land cover classification (Broxton et al., 2014), defines 7 regions: "water", "forest", "savanna/shrub-land", "grassland/cropland", "urban", "snow" and "barren". The second method defines areas as custom polygons, named according to their geographical context. For this method, eight regions were defined: "cont_europe", "sahara_desert", "arabian_peninsula", "far_east_deserts", "persia", "india", "north-sahara_cropland" and "sahel". The different location times obtained from FLEXPART at each time and height step are summed for each region (land cover class and polygon), where the air parcel was below 1 km. The air mass source contributions are done by selecting only the air mass source profiles that are temporally close to lidar measurements selected. A time threshold less than one hour is used for these statistics.

3.4.3. The non-hydrostatic multiscale model of the Barcelona Supercomputing Center

The Non-hydrostatic Multiscale Model of the Barcelona Supercomputing Center (NMMB/BSC-Dust; Pérez et al., 2006, Pérez et al., 2011, Haustein et al., 2012) is a multi-scale atmospheric dust model embedded into the Non-hydrostatic Multiscale Model (NMMB) developed by the National Center for Environmental Prediction (NCEP, Janjic et al., 2011). It provides mineral dust forecasts for both regional and global domains. At a regional scale, the model reproduces the daily variability and seasonal spatial distribution of the dust optical depth over Northern Africa, the Middle East, and Europe. The maps of the aerosol optical depth caused by mineral dust are prepared in 0.1 × 0.1-degree resolution, covering a square geographical region from 0° to 65°N and 25° W to 65°E. The model is run daily at 12:00 UTC and gives a 72 h forecast with a separate map valid for every 3 h. The dust forecast archive (available via https://dust.aemet.es/products/daily-dust-products; last access on 12.05.2023), was examined using forecasts runs on 10–11.06.2019, to assess the likeliness of the mineral dust occurrence over Poland.

3.4.4. The Navy Aerosol Analysis and Prediction System (NAAPS)

The Navy Aerosol Analysis and Prediction System (NAAPS) reanalysis at 1 × 1-degree resolution and six-hourly maps that include aerosol mass concentration and optical properties (Lynch et al., 2016) is

used to analyse the temporal variability of aerosol properties. This reanalysis utilizes a modified version of the NAAPS, as its core and the 1-D module assimilates quality-controlled retrievals of AOD at 550 nm from the Moderate-Resolution Imaging Spectroradiometer (MODIS) onboard Terra/Aqua land and sea satellites, and the Multi-angle Imaging SpectroRadiometer (MISR) onboard a Terra satellite (Zhang et al., 2014). The NAAPS maps of the total aerosol optical depth (AOD at 550 nm) were used for the Europe domain with different tracers: mineral dust, sulfates, and smoke. For our research, the maps for 10–11.06.2019 were analysed (website: https://www.nrlmry.navy.mil/aerosol/index_frame.html; last access 12.05.2023).

4. Results and discussion

In terms of lidar data, mineral dust aerosol inflow is likely when strong particle backscattering is accompanied by increased particle depolarization at a certain layer (e.g. Shin et al., 2018; Szczepanik et al.,

2021, 2022). Such type of aerosol was documented as measured in a very complicated meteorological situation with collocated lidar, cloud radar, and radiometer by Wang et al., 2020. By doing this, a newly developed aerosol-cloud typing algorithm revealed unambiguously an occurrence of mineral dust over Rzecin, which triggered the selection of a case study for our research. The lidar quick-look plots in Warsaw and Rzecin, available via the PolandAOD website, revealed the possible occurrence of mineral dust observed simultaneously on 10–11.06.2019. The overview plots at both sites in Figs. 3 and 4, respectively, show the entire event and the periods used for direct comparisons (red boxes). The mineral dust layer observed over Rzecin was much stronger and wider (2.5–5 km, δ_V = 15–20 %) than the one observed in Warsaw (3.0–4.5 km, δ_V = 10–15 %).

The list of full sets of profiles of optical properties of atmospheric aerosol that were obtained using the SCC algorithms for Warsaw and Rzecin is given in Table 1. In Warsaw (Fig. 3), during the entire period clear sky conditions with some cirrus clouds above 9 km prevailed and a depolarizing layer of the aerosol was captured between 3 and 5 km. In such meteorological conditions it was possible to obtain 12 full sets of profiles in Warsaw. In Rzecin (Fig. 4), the weather situation was more complex and dynamic with clouds at different levels and stronger aerosol load, and therefore here data evaluation was more challenging. The SCC cloud mask did not improve results in terms of low cloud filtering, which is consistent with issues reported during the Near Real-Time COVID-19 EARLINET – ACTRIS campaign (Nicolae et al., 2020). These meteorological conditions in Rzecin lead to 8 full sets of profiles of optical properties of atmospheric aerosol (Table 1).

The SCC provides for each set of profiles the data products with different vertical resolutions, depending on the signal-to-noise ratio. Therefore, to perform comparative analyses the obtained sets of profiles were smoothed using the running mean, so as to get comparable vertical resolution. For the PollyXT lidar, the smoothing window was of 367.5 m for the β, δ_p, WV and Angstrom exponent related to backscattering AE_β and 757.5 m for α, LR and Angstrom Exponent related to extinction AE_α. In case of the EMORAL lidar, the smoothing applied was the same for every profile and equal 367.5 m. This enabled, on the one hand, a direct comparison of the properties between two almost identical time spans selected for the two sites, and on the other hand, an analysis focused on spatio-temporal tracking of changes during the evolution of the mineral dust inflow event at each site. This was done with a strong emphasis on
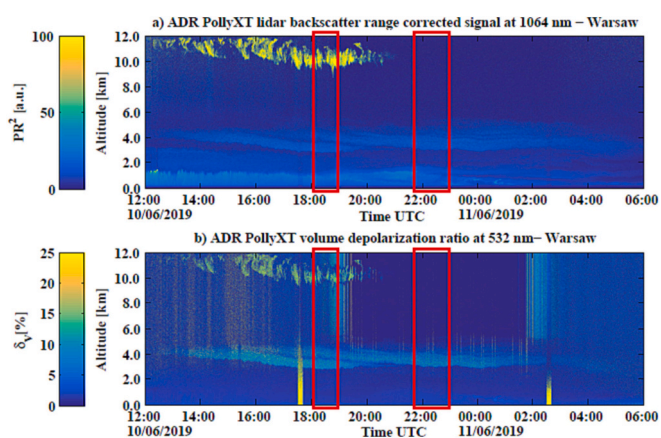

Fig. 3. Quick look plots for PollyXT lidar of range corrected signal PR^2 at 1064 nm (upper panel) and linear volume depolarization δ_V at 532 nm (lower panel) measured by PollyXT lidar at the RS-Lab site in Warsaw. Red boxes define the periods of interest (G1 and G2). Layer of mineral dust aerosol is marked by increased δ_V at 3–5 km, high-level cirrus clouds >9 km were observed only in the evening, then clear sky conditions are captured over the night.
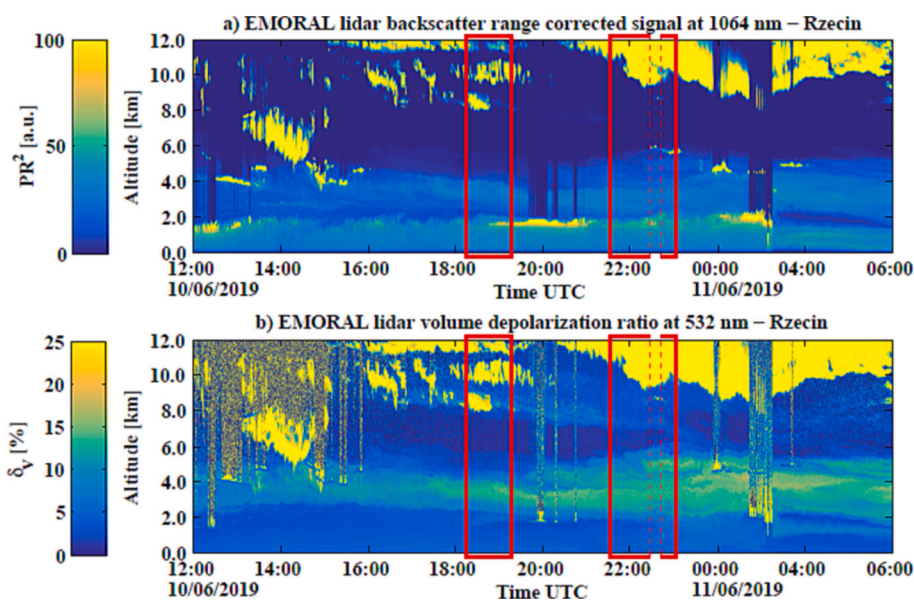

Fig. 4. Quick look plots of range corrected signal PR^2 at 1064 nm (upper panel) and linear volume depolarization δ_V at 532 nm (lower panel) measured with EMORAL lidar at the PolWET site in Rzecin. Red boxes mark G1 and G2 periods. Dynamic meteorological situation with a wide layer of depolarizing aerosol at 2–6 km and cirrus clouds in the upper free troposphere.

the aerosol properties derived within the observed dust layers at both sites.

The two-step POLIPHON separation algorithm applied on the profiles of both lidars listed in Table 1 revealed significant differences in terms of the fine and coarse mode dust presence at both sites depicted in Figs. 9 and 10. The mineral dust layer in Warsaw (Fig. 5) was at first appearing as a thin layer having <1.7 km thickness (profiles 1–3), then it was becoming more spread out, reaching >2.5 km in the vertical direction. As for the observed mineral dust composition, at the first stage, the fine mode fraction of mineral dust particles dominates over the coarse mode. After 20:50 UTC at 10.06.2019 (Fig. 5, profile no. 8), both modes were in balance (mainly in the lower part of the observed layer). The fraction contribution changed after the 01:05 (Fig. 5, profile no.12), when amount of coarse mode particles started to decline. The dust layer evolution over Rzecin (Fig. 6) was significantly different with the aerosol layer very wide in a vertical direction for every profile. The coarse mineral dust fraction was dominating over fine mode fraction, after 21:45 UTC, 10.06.2019 (Fig. 6, profile no. 6), in the upper part of dust layer (above 3.5 km). Moreover, there was a contribution of the fine mode mineral dust particles even within boundary layer (BL) – not investigated in this study. In the free troposphere (FT) fine mode dominated initially, and then gradually decreased starting from 21:00 UTC 10.06.2019 (Fig. 6, profile no. 5).

4.1. Comparative analyses of mineral dust properties in G1 and G2 groups

Within this section we discussed all available parameters of the optical properties of aerosol within the mineral dust layers. In case the optical property was not derived it is explicitly given.

The mineral dust inflow observed simultaneously over the Warsaw and Rzecin sites on 10–11.06.2019 was analysed with reference to two selected periods chosen when the obtained vertical profiles of the atmosphere for those two sites had similar time averaging and started almost at the same time of a day, denoted as G1 and G2 (Figs. 3-10, Table 1). Note that we will discuss sets of optical properties for both groups but we show the profiles only for G2 for brevity.

The aerosol optical properties obtained for the Warsaw site for the first period of interest (G1: 18:05–18:50 UTC on 10.06.2019) were characterized with a strongly depolarizing, inhomogeneous aerosol layer at 3.0–5.3 km with two local maxima at 3.6 km with δ_p of 16 ± 0.5
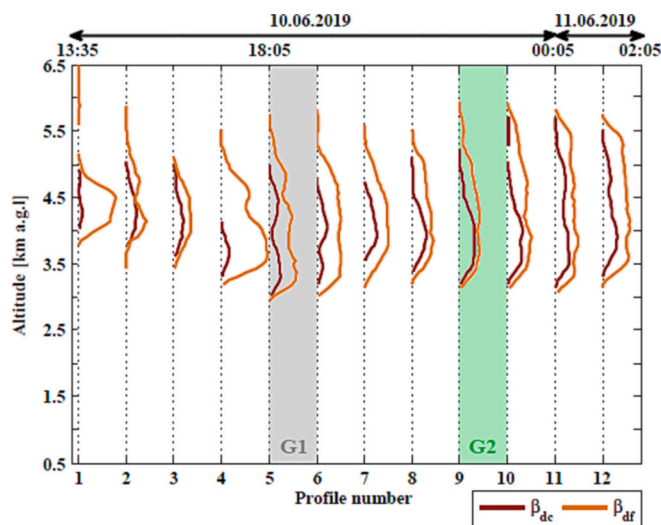

Fig. 5. Evolution of the mineral dust event in terms of the fine and coarse mode dust obtained using the POLIPHON two-step separation for the particle backscatter coefficient derived from PollyXT lidar with Raman method on 10–11.06.2019 in Warsaw. Profile numbers correspond to times given in Table 1, as well as G1 and G2, which indicate profiles used for direct comparisons.

% and at 4.5 km, where δ_p was of 15 ± 1 %. The backscattering β values in the dust layer increased to $(0.64 \pm 0.10) \times 10^{-6} \text{m}^{-1}\text{sr}^{-1}$ at 1064 nm, $(1.10 \pm 0.15) \times 10^{-6} \text{m}^{-1}\text{sr}^{-1}$ at 532 nm and $(2.85 \pm 0.32) \times 10^{-6} \text{m}^{-1}\text{sr}^{-1}$ at 355 nm. The particle extinction coefficient α at 532 nm reached $(0.45 \pm 0.15) \times 10^{-4} \text{m}^{-1}$, while the lidar ratio LR at 532 nm was 40 ± 8 sr. The α at 355 nm was not derived at the height of the dust layer, so the lidar ratio LR at 355 and extinction Angstrom Exponent AE_α are only available within the boundary layer. In the dust layer, the backscatter Angstrom Exponent AE_β for each combination of wavelengths was similar ($0.90 + 0.10$) and lower than within the boundary layer, and thus, the layer was likely to contain large particles. Values of optical properties within the given uncertainties are in agreement with those reported for mineral dust (Nisantzi et al., 2015; Shin et al., 2018; Szczepanik et al., 2020; Szczepanik et al., 2021).

Table 1

Time periods used for calculation of the full sets of profiles of optical properties of atmospheric aerosol using EARLINET-ACTRIS Single Calculus Chain obtained for the Warsaw and Rzecin sites during mineral dust inflow on 10–11.06.2019. Profiles in grey (G1) and green (G2) indicate times used for direct comparisons.

| No.	Time Frames for Warsaw	No.	Time Frames for Rzecin
	10.06.2019		
1	13:25 – 14:25 (60 min)	-	Low clouds occurrence
2	14:25 – 15:25 (60 min)		
3	15:25 – 16:25 (60 min)	1	16:00 – 16:44 (44 min)
4	16:25 – 17:25 (60 min)	2	16:45 – 17:30 (45 min)
	17:30 – 17:45 (Polarization calibration)	3	17:30 – 18:14 (44 min)
5	**18:05 – 18:50 (45 min) - G1**	**4**	**18:15 – 19:14 (59 min) - G1**
6	18:50 – 19:50 (60 min)	-	Low clouds occurrence
7	19:50 – 20:50 (60 min)		
8	20:50 – 21:50 (60 min)	5	21:00 – 21:44 (44 min)
9	**21:50 – 22:50 (60 min) - G2**	**6**	**21:45 – 22:28 (43 min) - G2**
		7	**22:37 – 22:52 (15 min) - G2**
10	22:50 – 23:50 (60 min)	8	23:13 – 23:37 (24 min)
		9	23:39 – 23:53 (14 min)
	11.06.2019		
11	00:05 – 01:05 (60 min)	-	Low clouds occurrence
12	01:05 – 02:05 (60 min)		
-	No measurement		08:00 – 08:15 (Polarization calibration)
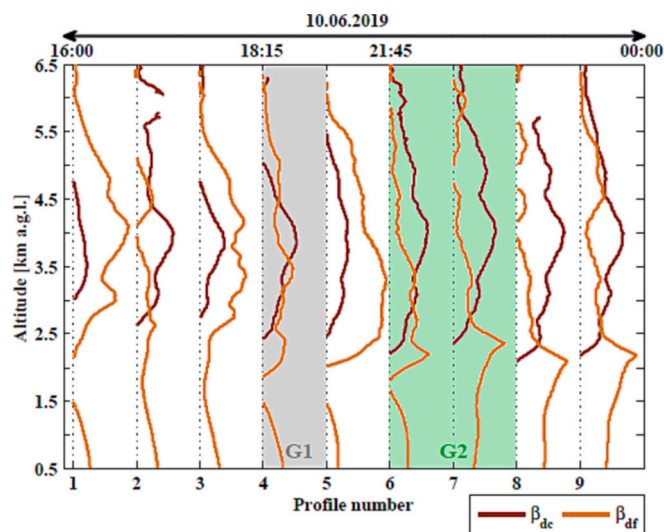
Fig. 6. Evolution of the mineral dust event in terms of the fine and coarse mode dust obtained using the POLIPHON two-step separation for the particle backscatter coefficient derived from EMORAL lidar with Raman method on 10–11.06.2019 in Rzecin. Profile numbers correspond to times given in Table 1. G1 and G2 indicate profiles used for direct comparisons.

For the corresponding period, the optical properties of mineral dust observed over Rzecin (G1: 18:15–19:14 on 10.06.2019) show a strongly depolarizing layer of aerosol observed between 2.5 and 5.8 km altitude that is wider in the vertical direction and more homogenous than in Warsaw, with a slightly higher δ_p at 532 nm of 17 ± 2 %. Between 1.5–2.1 km and 4.9–5.4 km values of δ_p at 532 nm are lower 10 ± 1 % and 13 ± 1 %, respectively. Within the depolarizing layer the β coefficients show raised values of $(1.8 \pm 0.25) \times 10^{-6}$ m^{-1}sr^{-1} at 1064 nm, $(1.4 \pm 0.20) \times 10^{-6}$ m^{-1}sr^{-1} at 532 nm and $(1.6 \pm 0.40) \times 10^{-6}$ m^{-1}sr^{-1} at 355 nm. The highest values of β at 1064 nm suggest the occurrence of large particles, which is in agreement with very low values

of AE$_\beta$ (oscillating around 0). The α at 355 nm within the dust layer reaches $(0.75 \pm 0.2) \times 10^{-4}$ m^{-1} (α at 532 nm is available only within the boundary layer). LR at 355 nm is reaching 32 ± 7 sr being in agreement with values reported for mineral dust over Warsaw (e.g. Szczepanik et al., 2021).

As for the second period in Warsaw (G2: 21:50–22:50 UTC on 10.06.2019; sets of profiles depicted in Fig. 7) the layer of enhanced δ_p between 3.1 and 5.6 km became more homogenous than for the G1 period. The δ_p reached maximum with 21 ± 1 % at 4.0 km and above 4.5 km decreased to 15 ± 2 %. The values of δ_p within the boundary layer were low (3.5 ± 0.5 %) and typical for the Warsaw station (Wang et al., 2019). Similarly as for G1, the dust layer was visible in β. Between 3.5 and 4.3 km larger particles occurred - β at 1064 nm increased to $(0.85 \pm 0.10) \times 10^{-6}$ m^{-1} sr^{-1}, which were captured by lower AE$_\beta$ (oscillating around 0). Within this layer β at 532 and 355 nm remain almost the same $(1.30 \pm 0.10) \times 10^{-6}$ m^{-1} sr^{-1} and $(1.32 \pm 0.30) \times 10^{-6}$ m^{-1} sr^{-1}, respectively. The α at 355 nm had two maxima at 3.7 km $(0.77 \pm 0.10) \times 10^{-4}$ m^{-1} and at 4.4 km $(1.00 \pm 0.12) \times 10^{-4}$ m^{-1}, but α at 532 nm only one at 4.0 km of $(0.83 \pm 0.10) \times 10^{-4}$ m^{-1}. Within the dust layer LRs are of 48 ± 18 sr and 49 ± 10 sr at 355 and 532 nm, respectively. Such values (within an error) are in agreement with values reported for mineral dust (Soupiona et al., 2020; Szczepanik et al., 2020; Szczepanik et al., 2021).

During this period, the optical properties in Rzecin (G2: 21:45 to 22:52 UTC on 10.06.2019; Fig. 8) were similar as in group G1 with the wide and homogeneous dust layer (see the profile of δ_p in Fig. 8, central panel), and still much wider than dust layer over Warsaw (Fig. 7). The core of the dust layer was at 2.2–6.0 km with a slightly higher particle depolarization than in G1 for Rzecin and almost the same as in G2 for Warsaw (δ_p of 22 ± 3 % at 532 nm). Within the dust layer, all β show raised values of $(1.1 \pm 0.2) \times 10^{-6}$ m^{-1} sr^{-1} at 1064 nm, $(1.8 \pm 0.20) \times 10^{-6}$ m^{-1} sr^{-1} at 532 nm and $(1.5 \pm 0.10) \times 10^{-6}$ m^{-1} sr^{-1} at 355 nm. The highest β at 532 nm may suggest the occurrence of larger particles, which is confirmed with mean AE$_{\beta(532/1064)}$ of 0.3 ± 0.1 and AE$_{\beta(355/1064)}$ of 0.8 ± 0.15. The α at 355 nm within the dust layer was reaching $(0.4 \pm 0.1) \times 10^{-4}$ m^{-1} (α at 532 nm covered altitudes <4.0 km only).
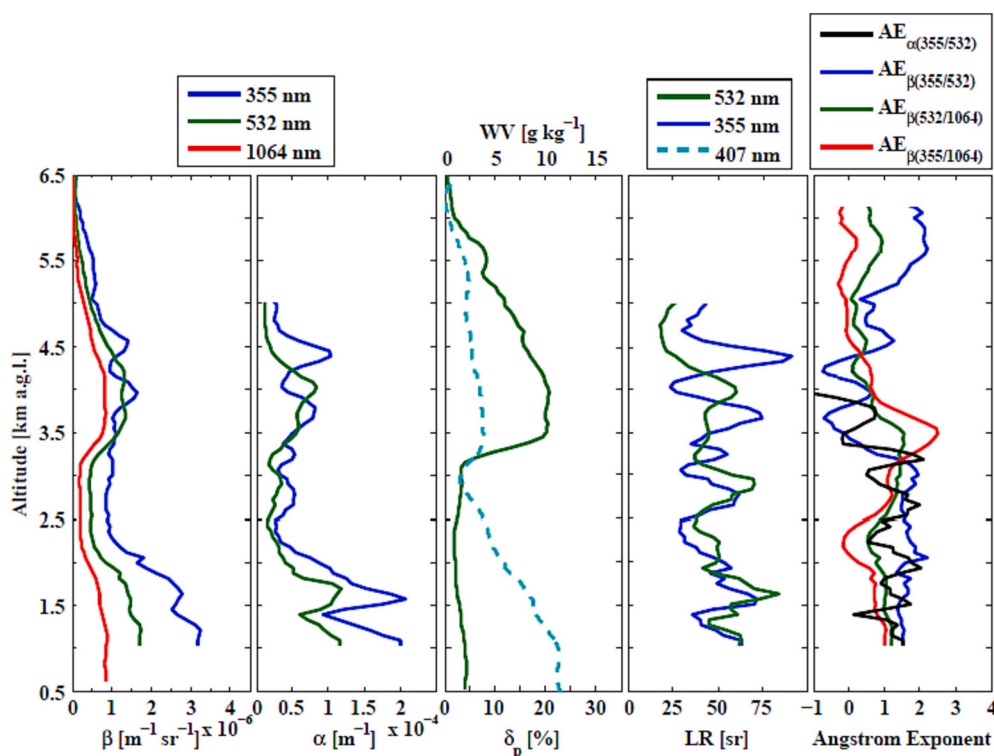

Fig. 7. Group 2 (G2) optical properties from PollyXT lidar in Warsaw – measurements from 21:50–22:50 UTC on 10.06.2019. The first panel (starting from left) shows the particle backscattering β at 355 (blue), 532 (green) and 1064 nm (red), then particle extinction profiles α at 355 (blue) and 532 nm (green). The central panel shows the particle linear depolarization ratio δ_p at 532 nm and water vapour mixing ratio WV at 407 nm (light blue). Lidar Ratios LR at 355 and 532 nm and Angstrom Exponent (extinction – AE$_\alpha$, and backscattering - AE$_\beta$-related) are depicted on the last two panels. Profiles with 60 min time averaging, 367.5 m vertical smoothing for β and β-related profiles, and 757.5 m vertical smoothing for α and α-related profiles.
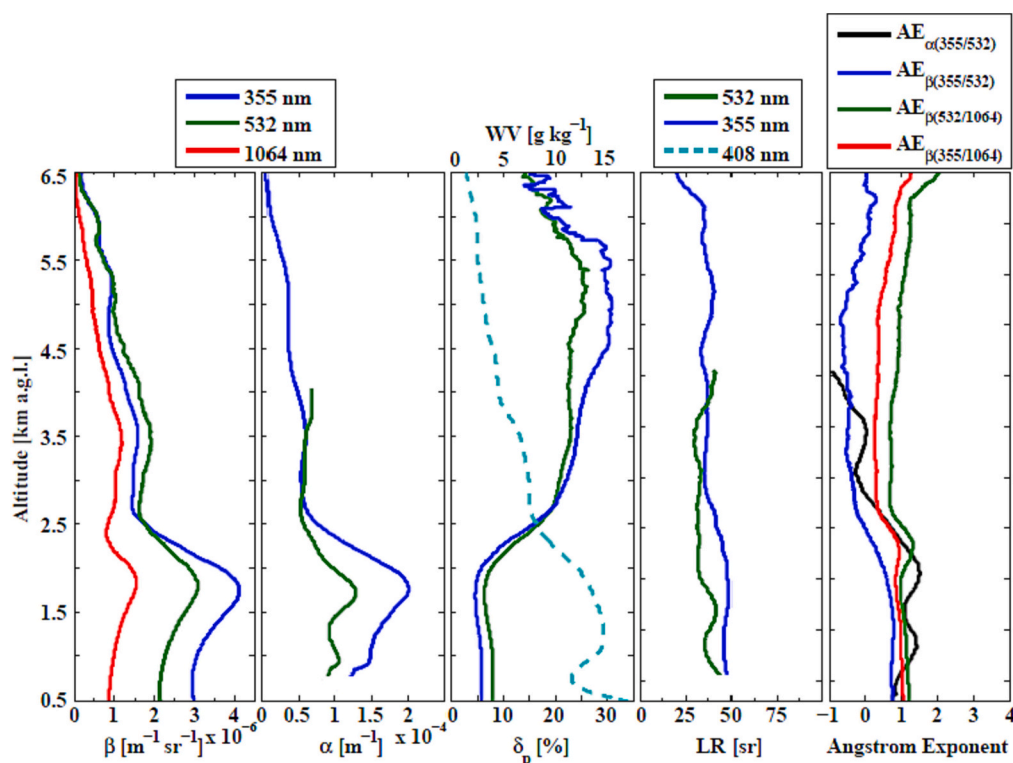
Fig. 8. Group 2 (G2) optical properties from EMORAL lidar in Rzecin – mean of 2 measurements from 21:45 UTC to 22:52 UTC on 10.06.2019. Panels same as in Fig. 7. Profiles with 59 min time averaging and 367.5 m vertical smoothing. To facilitate easy comparison with Fig. 7, the graphs are kept on the same scale of parameter variability.

Obtained mean AE_α < 2.5 km and at 2.8–4.0 km decreased from almost 1.2 ± 0.2 to -0.5 ± 0.2 respectively, which indicates the larger particles in the dust layer than those observed within the boundary layer. LR at 532 nm and at 355 nm was oscillating at 39 ± 6 sr.

In the case of Warsaw, there is a significant difference between the properties of observed aerosol layers and within discussed groups. The aerosol layer became more homogenous and was characterized by higher values of δ_p (increase from 15 to 16 % up to 21 %). This might be caused by the changes in the intensity of the transport and the rising amount of aerosol suspended in the air. Note that the G1 group is in the initial phase of the event, while G2 stays for the fully developed inflow (similar to the case described by Szczepanik et al., 2021). Interestingly, the α_p coefficient at 355 nm shows two local maxima – one slightly above the layer bottom, while the second in the so-called core of the

mineral dust layer. The lower maxima might be caused by the admixture of local pollution, while the second one is strongly connected to the observed mineral dust. Peaks in α_p at both wavelengths within the boundary layer occur at the exact same height, notable that it is not the case for the dust layer. It cannot be excluded that this is partly due to averaging aspect.

The main scope of our work is on the long-range transported mineral dust in the free troposphere. However, obviously for both sites, the β_p and α_p coefficients take the highest values within boundary layer (below 2 km), than within discussed layers (Figs. 7 and 8). A large amounts of aerosol of different types suspended within the atmospheric boundary layer is typical.
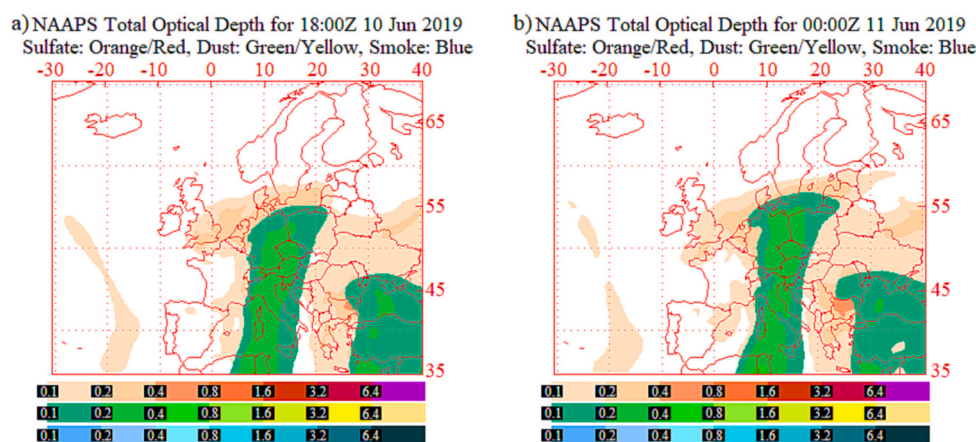

Fig. 9. The NAAPS model forecast of the aerosol optical depth of mineral dust (green/yellow), sulfates (orange/red), and smoke (blue) for a) 18:00 UTC 10 June 2019, and b) 00:00 UTC 11 June 2019, valid for the next 6 hours.

4.1.1. Models

For G1 and G2 aerosol source and type was interpreted with the use of HYSPLIT, FLEXPART, NAAPS (Fig. 9), and NMMB/BSC-Dust (shown in Figs. 10-11) models.

For both groups the NAAPS model (Fig. 9), https://www.nrlmry.navy.mil/aerosol/#aerosolobservations; last access 11.07.2023, shows significant AOD due to mineral dust (AOD_{dust} of 0.2–0.8), formed as a plume covering the central part of Europe on the transport pathway from North Africa (covering Italy, Austria, the Czech Republic, almost the whole of Germany, and more than half of Poland (including the western part and in particular Rzecin). AOD over Warsaw seems not being affected by mineral dust, but it is lying close to the dust plume border. There is no evidence of smoke aerosol, only some sulfates contribution over Europe ($AOD_{sulfates}$ of 0.1–0.2).

Similar results were obtained as an output of the NMMB\BSC-Dust model (Figs. 10-11); https://dust.aemet.es/forecast; last access on 10.05.2023). AOD caused by mineral dust was predicted over Central Europe, covering Western Poland (in particular over Rzecin), but not over Warsaw. We observe that both models (NAAPS and NMMB\BSC-Dust) underestimate the extent of this dust event over Central Poland, as it was measured over Warsaw with lidar but is not captured by the models. This problem of models underestimation of mineral dust occurrence was brought up in e.g. Adebiyi and Kok (2020) and by Huang et al., 2021. On the other hand, the results obtained from both models can partly explain observed differences between the size of dust plume over Poland. The layer detected over Rzecin is stronger than in Warsaw due to dust transport, which was more vivid over Western Poland and only residual over Central Poland.
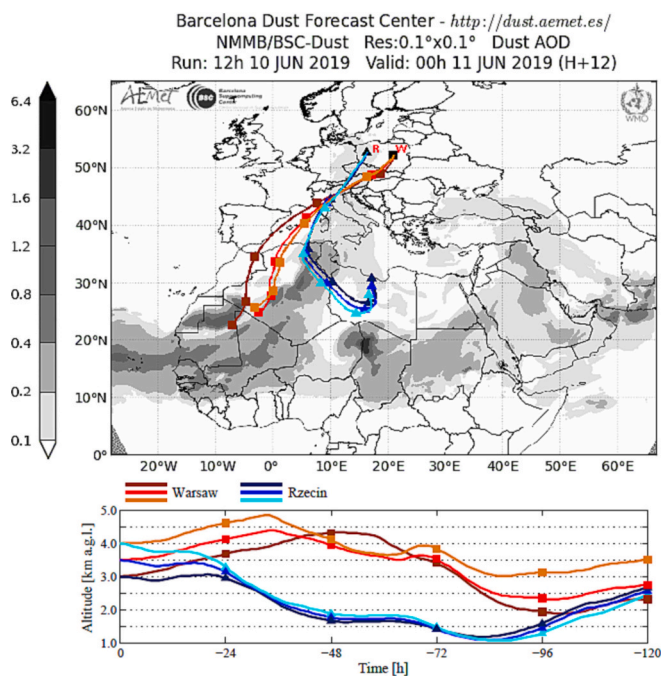

Fig. 11. AOD at 550 nm of mineral dust forecast with backward trajectories for the G2 group for both sites. NMMB/BSC-Dust model valid for 00:00 UTC on 11.06.2019. HYSPLIT model calculations for 120 h, starting at 22:00 UTC on 10.06.2019 (markers/colours as in Fig. 10). The forecast shows that the air masses from North Africa likely contained mineral dust. Backward trajectories indicate clearly different origins and no mixing.
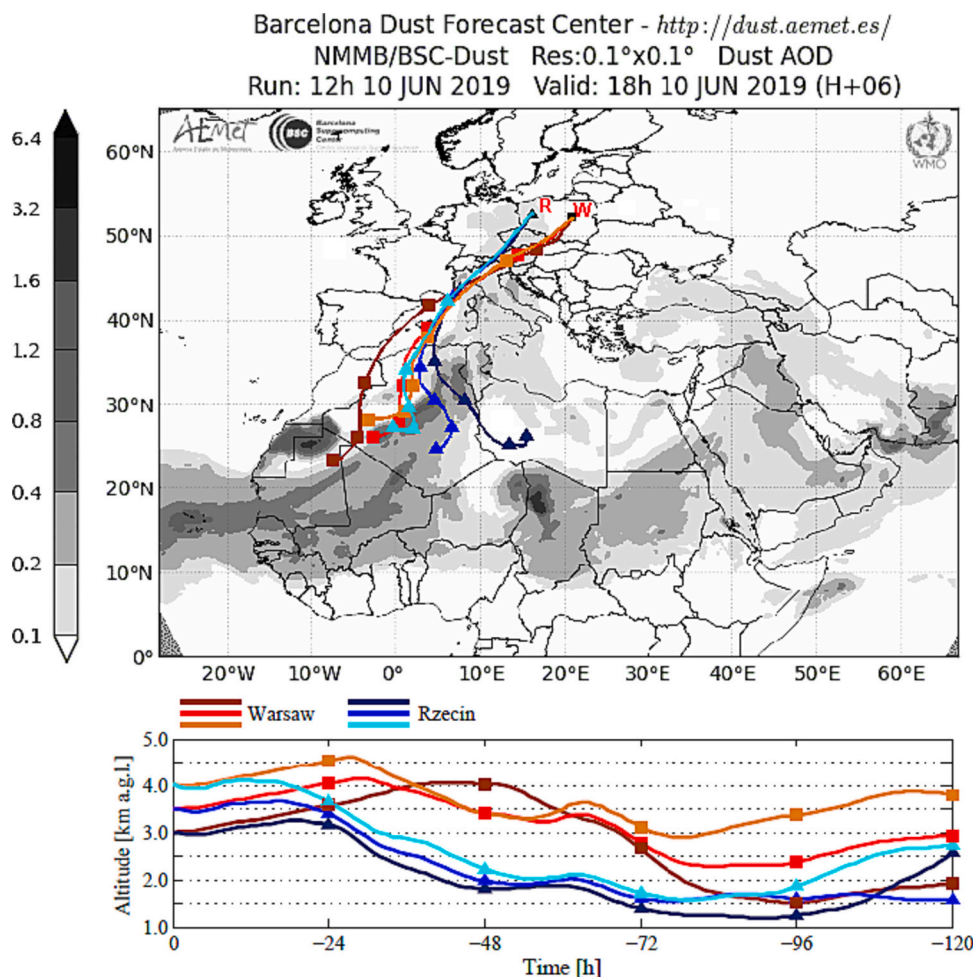

Fig. 10. Aerosol optical depth at 550 nm (AOD; grey shadow) of mineral dust forecast with superimposed backward trajectories for the G1 period for both sites on 10.06.2019. NMMB/BSC-Dust model run at 12:00 UTC valid for 18:00 UTC. HYSPLIT model calculations for 120 h, starting at 18:00 UTC at 3.0, 3.5, and 4.0 km a.g.l. Triangles/bluish lines for Rzecin (52.76 N, 16.31 E). Squares/reddish lines for Warsaw (52.21 N, 20.98 E). The forecast shows that the obtained air masses from North Africa likely contained mineral dust, whereby both were unlikely to mix.

Concerning the aerosol sources, relevant results were obtained from HYSPLIT backward trajectories analysis and TRACE statistics based on FLEXPART particle positions. The HYSPLIT analysis shows that the air-masses of North African origin were advecting to both sites independently, from different sources and without mixing (Figs. 10 and 11). Air-masses at the same altitude and time were separated from each other, which is the main reason for the differences in observed dust layers. Trajectory analysis also shows that the air was advancing the faster the closer to each station. Air mass source estimates, based on FLEXPART particles positions for the G1 and G2 periods for Warsaw and Rzecin are presented in Fig. 12 and in Fig. 13 respectively.

Note that for G2 the distinct aerosol source origin is even more confined to the different areas (Fig. 11). The only difference between G1 and G2 is that the sources of aerosol origins are even more separated, but still lying on the area of the Sahara desert. The sources estimation based on HYSPLIT backward trajectories analysis and TRACE analysis based on FLEXPART particle positions show considerable agreement. In all cases, both sites were highly influenced by the dust particles with a substantial fraction attributed to barren areas from the Sahara desert.

According to TRACE results for the G1 group presented in Fig. 12 (left panels), the aerosol layer above the 4 km height observed at Warsaw and the aerosol layer above the 3 km height observed at Rzecin are rich in mineral dust particles due to barren-ground-influenced air from the Sahara desert region. A small contribution from marine sources is also identified for the G1 group (Fig. 13, left panels).

For the layer between 2.8 and 3.9 km observed over Warsaw, marked with orange in the upper left panel of the Figs. 12 and 13, the marine source is dominant, with small contributions from the European and the African grass/cropland and savanna. For the G2 group, there is only one aerosol layer above 3.1 km height observed over the Warsaw site due to the change in wind direction. For this layer, barren regions from Africa are the main source; small fractions are attributed to water surface and African grass/cropland and savanna (upper right panel of the Figs. 12 and 13). The aerosol layer observed over Rzecin in the G1 and G2 periods is almost homogeneous, with air mass originating from the Sahara desert (bottom panels of the Figs. 12 and 13).

The optical parameters computed for these layers for the G1 and the G2 groups for both sites are typical for aerosol mixtures with a high dust fraction. The additional sulphate particles existing in the layers are associated with marine and continental sources contributions to long-range transported aerosols. This finding supports the observations presented by Talianu and Seibert (2019).

The difference in the aerosol optical properties observed are mostly linked to the history of the air masses sampled over station, being related to the mixing of dust (non-spherical) particles with continental pollution and/or biomass burning during transport - on the pathway of the air masses, MODIS spotted several fires in north Italy, Austria, and along the Polish-German border (based on the NASA World View maps (https://worldview.earthdata.nasa.gov/ last access 11.07.2023). Different air masses path ways to Rzecin and to Warsaw suggest that Rzecin was more
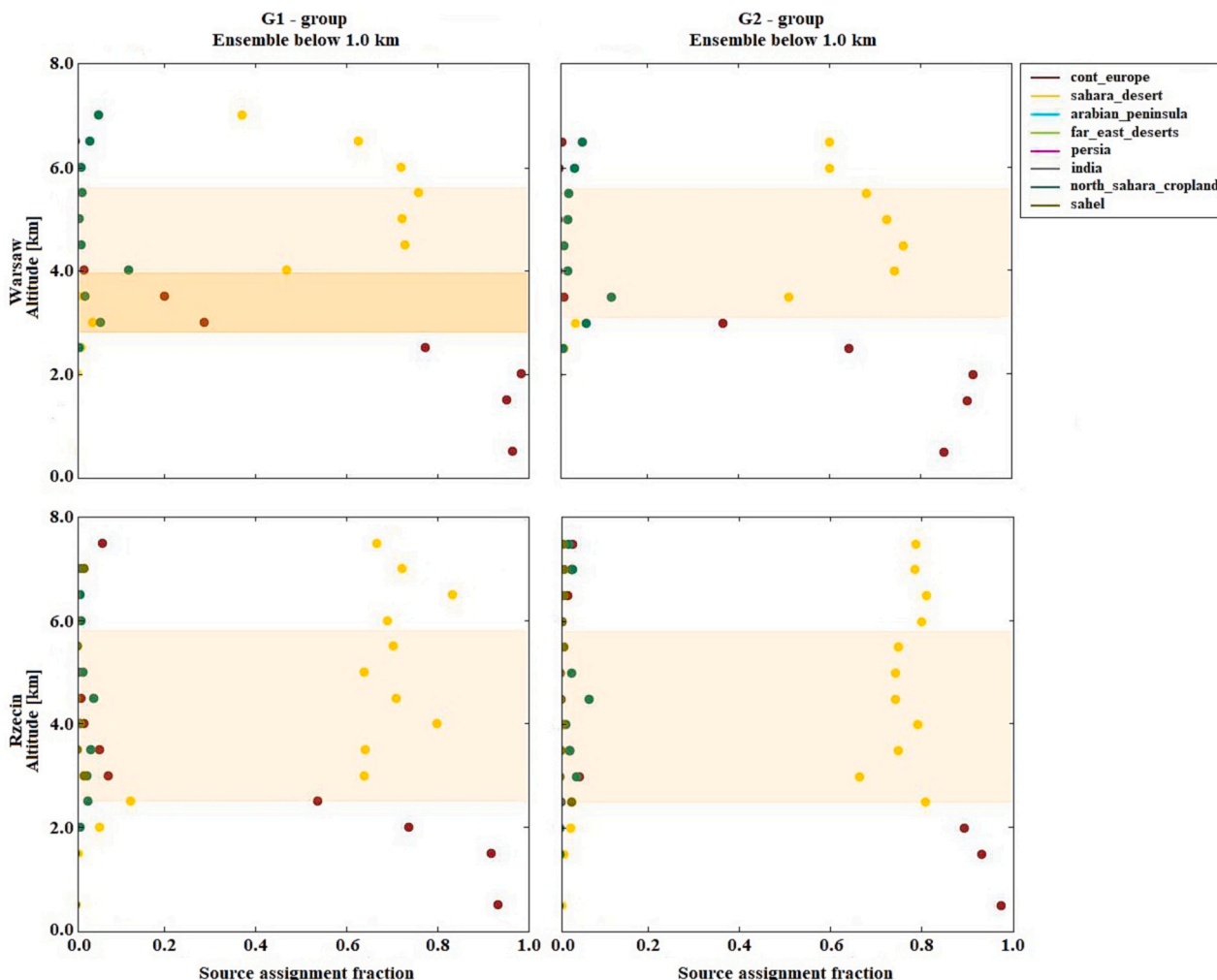

Fig. 12. Air mass source estimate for the land surface classification for FLEXPART simulations for the G1 group (left) and G2 group (right) for Warsaw (top) and Rzecin (bottom). Using the orangish and beige we marked the aerosol layer.
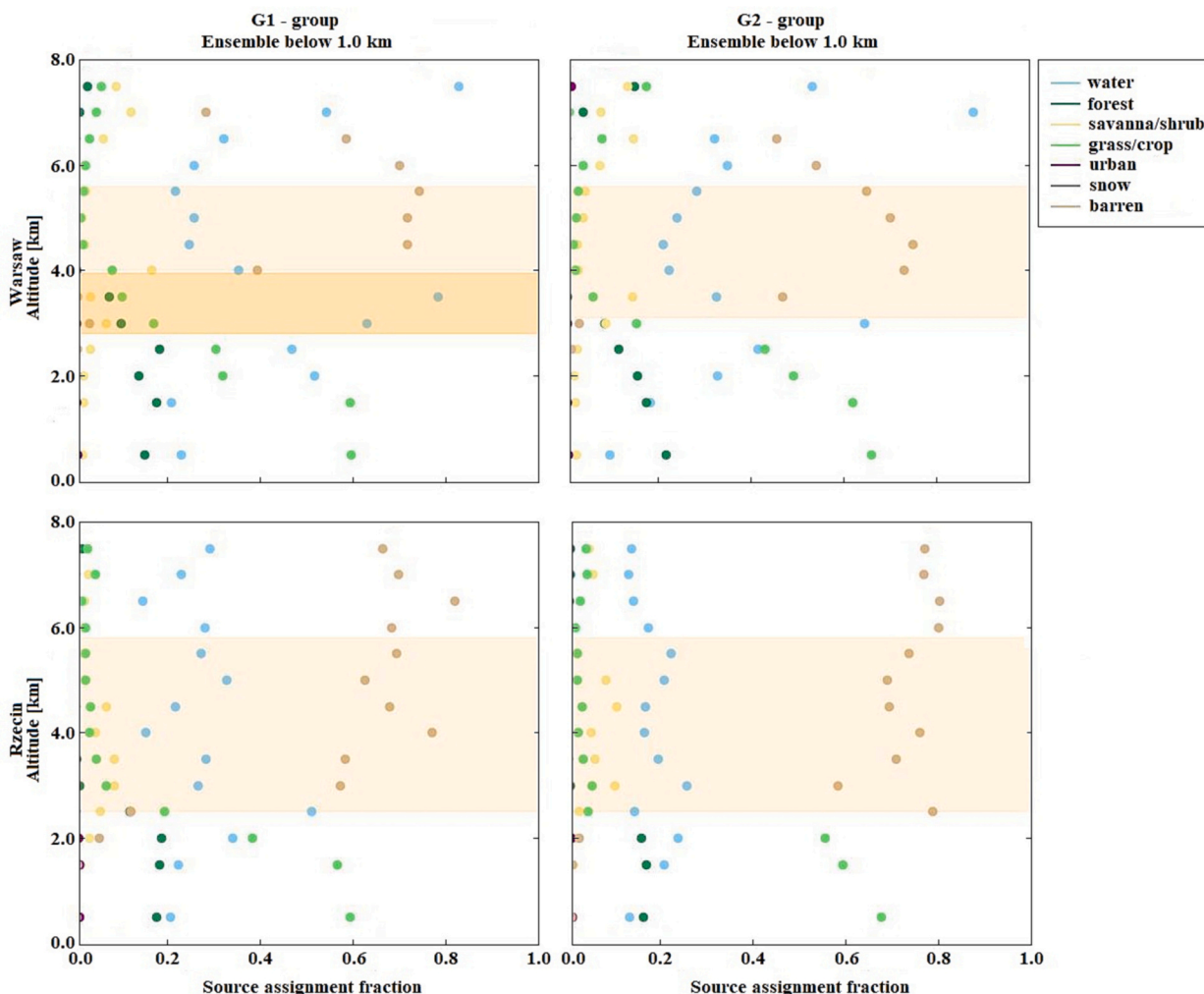
Fig. 13. Air mass source estimate for the land surface classification geographical areas (right) for FLEXPART simulations for the G1 (left) and G2 (right) groups for Warsaw (top) and Rzecin (bottom).

affected by the dust aerosol particles above the 3 km height.

4.2. Separation of mineral dust components

As the HYSPLIT and FLEXPART-TRACE results indicated more similarities between dust aerosol at both sites at the beginning (G1) and more discrepancies towards full development (G2) of the event we gave a closer look to see if the separation results are consistent with those results.

In Fig. 14, for G1 Warsaw (left plot, upper panel), the mineral dust accounts to 55 ± 5 % of β_{tot}, while for G1 Rzecin, it is slightly higher (63 ± 5 %). Also in terms of dust vertical distribution we see similarities, as the plum is only slightly wider in Rzecin. For G2 Warsaw and Rzecin separation results exhibits much more differences i.e. 63.5 % of β_{tot} stays for dust in Warsaw but in case of Rzecin it increases up to 74.5 %. Moreover the dust plum in Warsaw is becoming thinner while in Rzecin it widens even more.

For the G1 Warsaw the whole layer is clearly dominated by the fine dust particles (FCDR>0.55), with two minima (3.2–3.7 km and 4.4 km). Over G1 Rzecin the dust layer is also composed mainly of fine mode dust except for the minima at 4.0 km where fine and coarse dust contribute equally (FCDR~0.50). The increasing fine dust towards the bottom of the layer stays in agreement with aerosol typing results by Wang et al., 2020 (not shown for brevity, Fig. 5 therein). Moreover this result is consistent with the columnar sunphotometer retrievals (available only
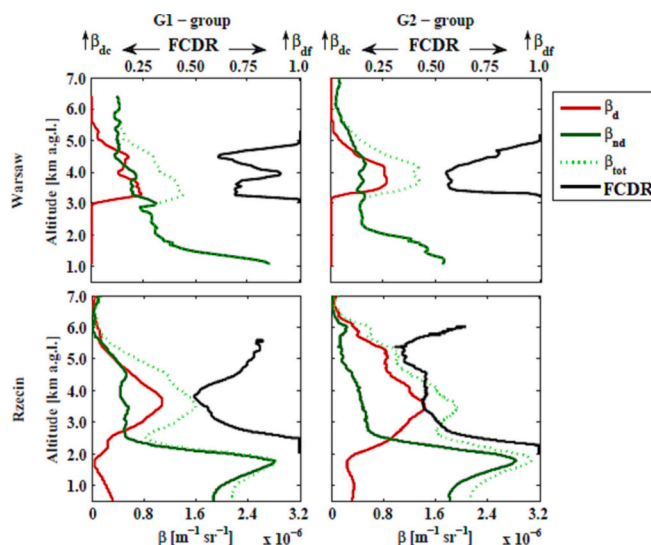

Fig. 14. Separation results for the G1 and G2 groups for both sites with FCDR marked. The upper panel presents results obtained for Warsaw while the lower one stays for Rzecin. The left side column represents the G1 results and the right one for G2. Information about dust (β_d - light brown line) and non-dust (β_{nd} - green line) contributions to the β profile at 532 nm (dotted green line) is given, as well as the FCDR (black line).
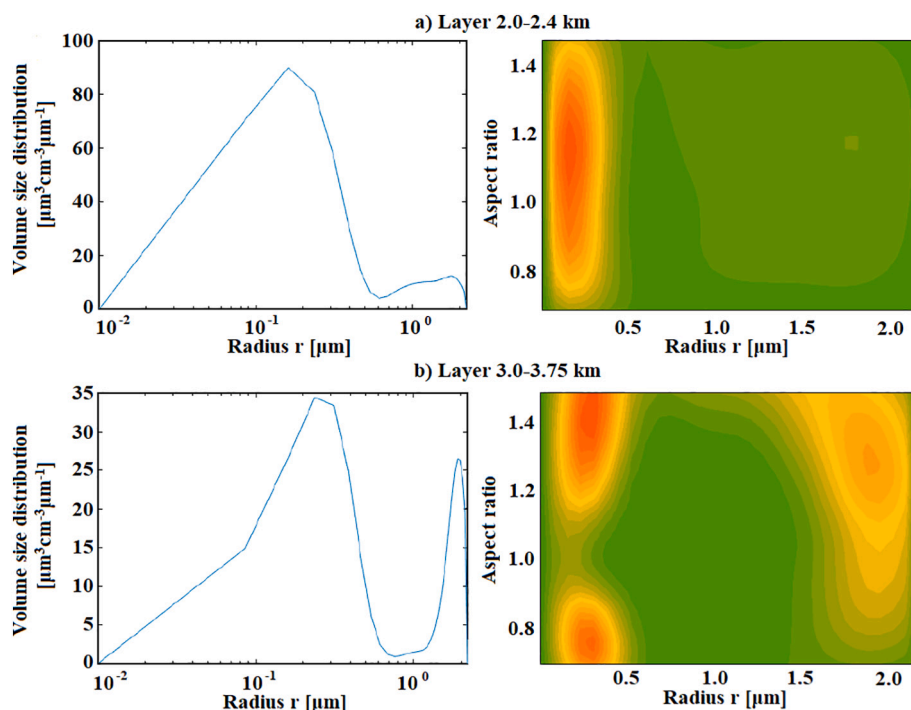
Fig. 15. Microphysical parameters for two layers from the G2 Rzecin group. The volume size distribution (left plots) and aspect ratio (right ones) inverted for a) layer at 2.0–2.4 km (lower δ_p, more spherical particles), and b) layer at 3.0–3.75 km (high δ_p, characteristic for mineral dust).

for G1 Warsaw). The mean daytime AODs was 0.40 at 340 nm and 0.095 at 1020 nm, with the values oscillating around average, with a tendency of rising during the day. The Ångström exponent started decreasing after 12 UTC from 1.47 to 0.9 – due to the mineral dust inflow. The aerosol size distribution obtained for a scan at 14:42 UTC (closest to G1 time) was bimodal, with a clear mode related to dust occurrence.

For the G2 Warsaw the aerosol layer is composed of fine and coarse dust particles between 3.4 and 4.0 km (FCDR of 0.50 ± 0.05). This stays in agreement with lower values of AE_β and increased β (Fig. 10). In contrast, more differences are seen for the G2 Rzecin, where the dust composition is with a stronger domination of coarse over fine dust particles. In the middle of the dust layer even more coarse particles were observed between 4.6 and 5.6 km, where the FCDR reaches a value of 0.37 ± 0.05.

For G2 Rzecin it was possible to invert the microphysical properties within two different altitude ranges, one within dust layer between 3.0 and 3.75 km, while the second (slightly below, from 2.0 to 2.4 km), consisting mainly of the spherical particles (low δ_p). The Pade-Iteration method (vi) with 30 iteration steps is almost always the most stable one which is known from extensive simulations. The results of the retrievals for both layers are on Fig. 15.

In case of the layer chosen with the mineral dust inflow, characterized with high particle depolarization ($\delta_p = 19.48 \pm 1.94$ % at 355 nm and 20.81 ± 1.14 % at 532 nm) the microphysical retrieval was made with the assumption of the nonspherical paricles. The distribution was bimodal with respect to the radius with the effective radius of 0.41 ± 0.13 μm. The particle radius was varying from 0.01 to 0.06 μm (aspect ratios 0.7–0.9 and >1.2) and 1.4–2.2 μm (aspect ratios >1.0), i.e., the distribution was bimodal with respect to the aspect ratio, too. Those results are in a good agreement with the separation results - the FCDR was 0.45, which indicates the domination of coarse mode particles but with the significant presence of fine mode fraction. The mean complex refractive index of $(1.5 + 0.028i) \pm (0 + 0.02i)$ and mean single scattering albedo of 0.81 ± 0.12 and 0.83 ± 0.11 at 355 nm and 532 nm respectively, indicate absorption with a significant standard deviation. Mean surface and volume concentration of 206.50 ± 26.36 μm^{2}cm^{-3}

and 32.75 ± 5.31 μm^{3}cm^{-3} was obtained.

In the second layer (with low δ_p of 5.27 ± 0.69 % and 6.45 ± 0.83 % for 355 and 532 nm respectively) the microphysical retrieval made with the assumption of mostly spherical particles, revealed that the distribution was single mode with the effective radius of 0.25 ± 0.02 μm. The particle radius was varying from 0.009 to 0.3 μm (aspect ratios 0.8–1.4). Within this layer the FCDR was decreasing with height (from 1 to 0.75 within the discussed layer), which is in agreement with the obtained microphysical results. The mean complex refractive index of $(1.47 + 0.04i) \pm (0.05 + 0.012i)$ and mean single scattering albedo of 0.78 ± 0.04 and 0.79 ± 0.04 at 355 and 532 nm respectively, indicate some absorption slightly higher than for the previously discussed mineral dust layer, but still standard deviation was sizable. Mean surface and volume concentration of 499.50 ± 34.31 μm^{2}cm^{-3} and 41.85 ± 1.00 μm^{3}cm^{-3} was obtained.

5. Conclusions

A comparative study of the mineral dust inflow over two measuring sites in Poland showed several significant differences, leading to the conclusion that aerosol influx can have different properties even on a small geographical scale (350 km). Such results support the necessity of extending the measuring infrastructure to a larger number of research stations, which can help to recognize the boundaries of events or the extent of their disappearance.

Aerosol prediction models (NAAPS, NMMB\BSC-Dust) underestimate or do not indicate at all the presence of mineral dust over some parts of Poland (and thus likely other areas of Central-Eastern Europe), as our lidar measurements gave undeniable evidence of the mineral dust presence over Poland during the analysed dust intrusion episode. It might be due to the different intensity of the mineral dust transport, that was significantly lower for Central than Western Poland. Consequently the size of the layer might have also played a role here. Thus the lidar data – if assimilated into the model – have strong potential to improve mineral dust occurrence predictions.

Additionally, the upcoming Earth Cloud Aerosol and Radiation

Explorer (EarthCARE) satellite mission of the European Space Agency (ESA, https://www.esa.int/Applications/Observing_the_Earth/FutureEO/EarthCARE, last access 22.05.2023) may both complete the models and be supplemented by the ground-based lidar measurements, so establishing a more dense network of lidar stations have many advantages.

A difference between obtained linear particle depolarization ratios δ_p (13 ± 3 % G1 Warsaw versus 17 ± 2 % G1 Rzecin, and 13 ± 1 % G2 Warsaw and 25 ± 3 % G2 Rzecin) is consistent with dust comparisons (more fine dust particles in Warsaw) and aerosol type (FLEXPART-TRACE) due to different aerosol origins (HYSPLIT) because air-masses were advected from different regions of North Africa. One has to keep in mind that dust suspended over Rzecin and Warsaw was to some extent hydrated differently at each site. In Warsaw WV ~ 3.0 g/kg-1 was consistent in the entire dust layer, while in Rzecin, it decreased with the height from 7.5 to 2.5 gkg-1, which resulted in lower depolarization and increasing fine fraction of mineral dust towards the bottom of the layer (Fig. 14, G1 Rzecin). The differences between particle depolarization and the dust particle fraction within observed aerosol layers would be even higher, if the moisture profile in Rzecin was more similar (drier) to what it was in Warsaw. The differences between humidity profiles are related to different climate conditions. Dry air over Warsaw is likely caused by the heat island conditions in an urban area. In contrast, the overgrowing lake with floating peat carpet causes a more humid environment over Rzecin.

Other extensive and intensive optical parameters such as particle backscattering β, particle extinction α coefficients, Angstrom Exponents - backscattering AE_β and extinction AE_α related, and lidar ratios LR are taking similar values, agreeing with values reported for mineral dust over Warsaw (Szczepanik et al., 2020, 2021, 2022) and other locations (Soupiona et al., 2020; Shin et al., 2018; Nisantzi et al., 2015). What has to be stressed, both lidar data analysis results contain coherent information on the dust particle sizes. AE_α close to the 0 and $AE_\beta < 1$ for both stations and groups of interest corresponds with higher values of β at higher detection wavelengths - for Warsaw β of $(1.30 \pm 0.10) \times 10^{-6}$ m^{-1} sr^{-1} and $(1.32 \pm 0.30) \times 10^{-6}$ m^{-1} sr^{-1} while for Rzecin $(1.8 \pm 0.20) \times 10^{-6}$ m^{-1} sr^{-1} and $(1.5 \pm 0.10) \times 10^{-6}$ m^{-1} sr^{-1} at 532 and 355 nm respectively.

Fine-to-coarse dust mode separation results showed an interesting evolution of the mineral dust layer observed over Warsaw and Rzecin, with more homogenous results in Warsaw. The G1 and G2 groups for both locations show differences in the case of the mineral dust fine and coarse particle fractions. At first (G1 group), the aerosol is composed mainly of fine particles with some contamination of coarse ones for both locations. For the G2 group in Warsaw, the layer is still dominated by fine particles but with a slightly higher amount of coarse ones than in the case of G1. For G2 Rzecin, the aerosol layer consists of a comparable amount of both fractions, with a rising amount of coarse particles in the upper part of the layer. This might be explained by the changes in the WV profile (discussed above).

The higher amount of fine particles observed over Warsaw than over Rzecin might be caused by the aerosol transport pathway. The backward trajectories calculated for Warsaw show that the air masses moved faster and from higher altitudes over the source area than the ones calculated for Rzecin (Figs. 10 and 11). Therefore the air masses over Warsaw are more likely to transport the fine dust, which could have been uplifted to higher altitudes. The source region of the Sahara desert may play a significant role here – the air masses observed over Warsaw originate from the western Sahara region, while over Rzecin is more from its central part. Additionally, small spherical pollution particles over Warsaw may decrease the values of δ_p."

The strongly visible fine dust aerosol layer suspended at the top of the boundary layer for the Rzecin station was also detected in the independent study of Wang et al., 2020. The detected aspherical particles within the boundary layer marked by POLIPHON algorithm as mineral dust are more likely related to pollination aerosol, which was well

captured by the TRACE - trajectories analysis tool.

The microphysical retrieval for the lower layer (considered as containing more spherical particles) is dominated by the particle from the accumulation mode with a small contributions from both giant and Aitken modes (particles of radius below 0.1 μm). It was possible that both giant and Aitken modes were present within the layer (good agreement between spherical and non-spherical models retrievals). Domination of the accumulation mode was expected since already the particle depolarization values indicates that presence of the aerosol mixture (mainly European aerosol background and a bit of mineral dust). Nevertheless the dust occurrence play significant role – it increases the effective radius and the imaginary part of the refractive index, and hence reduces the single scattering albedo values. In higher altitudes typically the wind speed is larger, hence an air advection from desert regions to central Europe quicker and more efficient. Here the giant mode is more prominent than in the lower layer and clearly prolate. The accumulation mode is slightly larger, than for previously discussed layer and may not be a uniform group of aerosol but consist both of prolate and oblate particles at the same time. Slightly surprisingly (despite of the more important giant mode, which of course probably is our dust component), the imaginary part of the refractive index is slightly lower, but still high. As the particles are even larger than before the single scattering albedo is slightly larger, but still remarkable low.

Our study revealed that both discussed aerosol prediction models failed to predict the mineral dust occurrence over Warsaw, while lidar measurements clearly indicated its presence. It was possible only thanks to the simultaneous observations at the two sites located in a distance of ~350 km. Moreover, this allowed to find the distinct pathways of air masses of different aerosol origin even on a such small scale (comparing to the distance from the source to the observation points). Therefore it is recommended to increase the number of high-quality multiwavelength lidar sites in Eastern Europe.

The lidar signals from both stations were evaluated using the classical Raman approach (Ansmann et al., 1990) for both night-time and daytime retrievals. Retrieval at daytime profiles is generally challenging due to sky-background radiation but feasible for ADR PollyXT lidar that was developed in a non-commercial collaboration of TROPOS and FUW (e.g. Janicka et al., 2017; Stachlewska et al., 2018; Wang et al., 2019). In this work we show that daytime Raman retrieval is achieved also for the EMORAL lidar built at Raymetrics in collaboration with research partners form LMU, UW, and NOA.

CRediT authorship contribution statement

Dominika M. Szczepanik: Formal analysis, Visualization, Data

curation, Validation, Funding acquisition, Writing – review & editing. **Patryk Poczta:** Formal analysis, Data curation, Writing – review & editing. **Camelia Talianu:** Formal analysis, Data curation, Validation, Funding acquisition, Writing – review & editing. **Christine Böckmann:** Formal analysis, Data curation, Validation, Funding acquisition, Writing – review & editing. **Christoph Ritter:** Formal analysis, Data curation, Writing – review & editing. **Horatiu Stefanie:** Validation, Investigation, Writing – review & editing. **Florica Toanca:** Validation, Investigation, Funding acquisition, Writing – review & editing. **Bogdan H. Chojnicki:** Validation, Investigation, Writing – review & editing. **Dirk Schütte-meyer:** Validation, Investigation, Funding acquisition, Writing – review & editing. **Iwona S. Stachlewska:** Conceptualization, Methodology, Writing – original draft, Validation, Investigation, Resources, Funding acquisition, Writing – review & editing.

Declaration of competing interest

The authors declare that they have no known competing financial interests or personal relationships that could have appeared to influence the work reported in this paper.

Data availability

Data will be made available on request.

Appendix A

Table A1
Single calculus chain settings for PollyXT and EMORAL lidar systems used for the optical products retrieval.

Optical property	PollyXT – Warsaw	EMORAL – Rzecin
Particle backscattering coefficient at 1064 nm	*Raman backscatter (000)*; Usecase: 7 Calibration range: 3.0–12.0 km Calibration value: 1.0 s0 Error: 50 %	*Raman backscatter (000)*; Usecase: 0 Calibration range: 3.0–10.0 km Calibration value: 1.05 Error for G1&G2: 5 % (<2 km), 20 % (>2 km)
Particle backscattering coefficient at 532 nm	*Lidar ratio and extinction (002)*; Usecase: 7 Calibration range: 3.0–12.0 km Calibration value: 1.00 Error: 50 % (<2 km), 100 % (>2 km)	*Raman backscatter and linear depolarization ratio (007)*; Usecase: 0 Calibration range: 3.0–10.0 km Calibration value: 1.05 Error for G1: 5 % (<2 km), 10 % (>2 km) Error for G2: 5 % (<2 km), 30 % (>2 km)
Particle backscattering coefficient at 355 nm	*Lidar ratio and extinction (002)*; Usecase: 7 Calibration range: 3.0–12.0 km Calibration value: 1.00 Error: 50 % (<2 km), 100 % (>2 km)	*Raman backscatter and linear depolarization ratio (007)*; Usecase: 0 Calibration range: 3.0–10.0 km Calibration value: 1.03 Error for G1&G2: 5 % (<2 km), 10 % (>2 km)
Particle extinction coefficient at 532 nm	*Lidar ratio and extinction (002)*; Usecase: 7 Calibration range: 3.0–12.0 km Calibration value: 1.00 Error: 50 % (<2 km), 100 % (>2 km)	*Lidar ratio and extinction (002)*; Usecase: 7 Calibration range: 3.0–10.0 km Calibration value: 1.05 Error for G1: 5 % (<2 km), 10 % (>2 km) Error for G2: 5 % (<2 km), 30 % (>2 km)
Particle extinction coefficient at 355 nm	*Lidar ratio and extinction (002)*; Usecase: 7 Calibration range: 3.0–12.0 km Calibration value: 1.00 Error: 50 % (<2 km), 100 % (>2 km)	*Lidar ratio and extinction (002)*; Usecase: 7 Calibration range: 3.0–10.0 km Calibration value: 1.03 Error for G1&G2: 5 % (<2 km), 10 % (>2 km)
Particle linear depolarization ratio at 532 nm	*Raman backscatter and linear depolarization ratio (007)*; Usecase: 0 Calibration range: 1.0–12.0 km Calibration value: 1.00 Error: 50 %	*Raman backscatter and linear depolarization ratio (007)*; Usecase: 0 Calibration range: 3.0–10.0 km Calibration value: 1.05 Error for G1: 5 % (<2 km), 10 % (>2 km) Error for G2: 5 % (<2 km), 30 % (>2 km)
Particle linear depolarization ratio at 355 nm	*Raman backscatter and linear depolarization ratio (007)*; Usecase: 0 Calibration range: 1.0–12.0 km Calibration value: 1.00 Error: 50 %	*Raman backscatter and linear depolarization ratio (007)*; Usecase: 0; Calibration range: 3.0–10.0 km Calibration value: 1.03 Error for G1&G2: 5 % (<2 km), 10 % (>2 km)

References

Adebiyi, A.A., Kok, J., 2020. F.: climate models miss most of the coarse dust in the atmosphere. Sci. Adv. 6 (15), eaaz9507 https://doi.org/10.1126/sciadv.aaz9507.

Ajtai, N., Ştefănie, H., Mereuţă, A., Radovici, A., Botezan, C., 2020. Multi-sensor observation of a Saharan dust outbreak over Transylvania, Romania in April 2019. Atmosphere 11, 364. https://doi.org/10.3390/atmos11040364.

Amato, F., D'Amico, G., Mona, L., Pappalardo, G., 2018. Report on the EARLINET Database Quality Control Procedures, Rapporto tecnico. Attivita di Ricerca,

Consiglio Nazionale delle Ricerche. http://www.cnr.it/istituti/ProdottoDellaRicerca.html?cds=055&id=389939.

Ansmann, A., Riebesell, M., Weitkamp, C., 1990. Measurement of atmospheric aerosol extinction profiles with a Raman lidar. Opt. Lett. 15 (13), 746–748.

Böckmann, C., Kirsche, A., 2006. Iterative regularization method for lidar remote sensing. Comput. Phys. Commun. 174, 607–615. https://doi.org/10.1016/j.cpc.2005.12.019.

Böckmann, C., Osterloh, L., 2014. Runge-Kutta type regularization method for inversion of spheroidal particle distribution from limited optical data. Inverse Prob. Sci. Eng. 22 (1), 150–165. https://doi.org/10.1080/17415977.2013.830615.

Broxton, P.D., Zeng, X., Sulla-Menashe, D., Troch, P.A., 2014. A global land cover climatology using MODIS data. J. Appl. Meteorol. Climatol. 53, 1593–1605. https://doi.org/10.1175/JAMC-D-13-0270.1.

Calidonna, C.R., Avolio, E., Gullì, D., Ammoscato, I., De Pino, M., Donateo, A., Feudo, T.L., 2020. Five years of dust episodes at the southern Italy GAW regional coastal mediterranean observatory: multisensors and modeling analysis. Atmosphere 11, 456. https://doi.org/10.3390/ATMOS11050456.

Chojnicki, B.H., Urbaniak, M., Józefczyk, D., Augustin, J., Olejnik, J., 2007. Measurements of gas and heat fluxes at Rzecin wetland. In: Okruszko, T., Maltby, E., Szatylowicz, J., Światek, D., Kotowski, W. (Eds.), Monitoring, Modeling and Management. Taylor & Francis Group, London, pp. 125–131.

D'Amico, G., Amodeo, A., Baars, H., Binietoglou, I., Freudenthaler, V., Mattis, I., Wandinger, U., Pappalardo, G., 2015. EARLINET single calculus chain – overview on methodology and strategy. Atmos. Meas. Tech. 8, 4891–4916. https://doi.org/10.5194/amt-8-4891-2015.

D'Amico, G., Amodeo, A., Mattis, I., Freudenthaler, V., Pappalardo, G., 2016. EARLINET Single Calculus Chain – technical – part 1: pre-processing of raw lidar data. Atmos. Meas. Tech. 9, 491–507. https://doi.org/10.5194/amt-9-491-2016.

Di Biagio, C., Balkanski, Y., Albani, S., Boucher, O., Formenti, P., 2020. Direct radiative effect by mineral dust aerosols constrained by new microphysical and spectral optical data. Geophys. Res. Lett. 47, e2019GL086186 https://doi.org/10.1029/2019GL086186.

Draxler, R.R., Rolph, G.D.. HYSPLIT (HYbrid Single-Particle Lagrangian Integrated Trajectory) Model Access Via NOAA ARL READY Website. http://ready.arl.noaa.gov/HYSPLIT.php.

Dubovik, O., Sinyuk, A., Lapyonok, T., Holben, B.N., Mischchenko, M., Yang, P., Eck, T.F., Volten, H., Munoz, O., Veihelmann, B., van der Zande, W.J., Leon, J.F., Sorokin, M., Slutsker, I., 2006. Application of spheroid models to account for aerosol particle nonsphericity in remote sensing of desert dust. J. Geophys. Res.-Atmos. 111, D11208. https://doi.org/10.1029/2005JD006619.

Engelmann, R., Kanitz, T., Baars, H., Althausen, D., Skupin, A., Wandinger, U., Komppula, M., Stachlewska, I.S., Amiridis, V., Marinou, E., Mattis, I., Linne, H., Ansmann, A., 2016. The automated multiwave-length Raman polarization and water-vapor lidar PollyXT: the neXT generation. Atmos. Meas. Tech. 9, 1767–1784. https://doi.org/10.5194/amt-9-1767-2016.

Feuerstein, S., Schepanski, K., 2019. Identification of dust sources in a Saharan dust hot-spot and their implementation in a dust-emission model. Remote Sens. 11, 4. https://doi.org/10.3390/rs11010004.

Formenti, P., Schütz, L., Balkanski, Y., Desboeufs, K., Ebert, M., Kandler, K., Petzold, A., Scheuvens, D., Weinbruch, S., Zhang, D., 2011. Recent progress in understanding physical and chemical properties of African and Asian mineral dust. Atmos. Chem. Phys. 11, 8231–8256. https://doi.org/10.5194/acp-11-8231-2011.

Freudenthaler, V., Linné, H., Chaikovski, A., Rabus, D., Groß, S., 2018. EARLINET lidar quality assurance tools. Atmos. Meas. Tech. Discuss. https://doi.org/10.5194/amt-2017-395 preprint. in review.

Groot Zwaaftink, C.D., Aas, W., Eckhardt, S., Evangeliou, N., Hamer, P., Johnsrud, M., Kylling, A., Platt, S.M., Stebel, K., Uggerud, H., Yttri, K.E., 2022. What caused a record high PM10 episode in northern Europe in October 2020? Atmos. Chem. Phys. 22, 3789–3810. https://doi.org/10.5194/acp-22-3789-2022.

Hansen, P.C., 2010. Discrete Inverse Problems: Insight and Algorithms. Society for Industrial and Applied Mathematics. https://doi.org/10.1137/1.9780898718836.

Hara, Y., Nishizawa, T., Sugimoto, N., Osada, K., Yumimoto, K., Uno, I., Kudo, R., Ishimoto, H., 2018. Retrieval of aerosol components using multi-wavelength Mie-Raman Lidar and comparison with ground aerosol sampling. Remote Sens. 10, 937. https://doi.org/10.3390/rs10060937.

Harenda, K.M., Samson, M., Juszczak, R., Markowicz, K.M., Stachlewska, I.S., Kleniewska, M., MacArthur, A., Schüttemeyer, D., Chojnicki, B.H., 2021. Impact of atmospheric optical properties on net ecosystem productivity of peatland in Poland. Remote Sens. 13, 2124. https://doi.org/10.3390/rs13112124.

Haustein, K., Pérez, C., Baldasano, J.M., Jorba, O., Basart, S., Miller, R.L., Janjic, Z., Black, T., Nickovic, S., Todd, M.C., Washington, R., Müller, D., Tesche, M., Weinzierl, B., Esselborn, M., Schladitz, A., 2012. Atmospheric dust modeling from meso to global scales with the online NMMB/BSC-dust model–part 2: experimental campaigns in northern Africa. Atmos. Chem. Phys. 12, 2933–2958. https://doi.org/10.5194/acp-12-2933-2012.

Hogan, T.F., Rosmond, T.E., 1991. The description of the navy operational global atmospheric prediction System's spectral forecast model. Mon. Weather Rev. 119 (8), 1786–1815.

Huang, Y., Adebiyi, A.A., Formenti, P., Kok, J.F., 2021. Linking the different diameter types of aspherical desert dust indicates that models underestimate coarse dust emission. Geophys. Res. Lett. 48, e2020GL092054 https://doi.org/10.1029/2020GL092054.

Huang, Z., Nee, J.-B., Chiang, C.-W., Zhang, S., Jin, H., Wang, W., Zhou, T., 2018. Real-time observations of dust–cloud interactions based on polarization and raman lidar measurements. Remote Sens. 10 (7), 1017. https://doi.org/10.3390/rs10071017.

IMGW-PIB, . The source of the data is the Institute of Meteorology and Water Management - National Research Institute. https://dane.imgw.pl/data/dane_pomiarowo_obserwacyjne/. In: Data From Szamotuły-Baborówko (No. 3203) Station of the Institute of Meteorology and Water Management - National Research Institute Have Been Processed. Polish Institute of Meteorology and Water Management - National Research Institute.

Janicka, L., Stachlewska, I.S., Veselovskii, I., Baars, H., 2017. Temporal variations in optical and microphysical properties of mineral dust and biomass burning aerosol derived from daytime Raman lidar observations over Warsaw, Poland. Atmos. Environ. 169, 162–174. https://doi.org/10.1016/j.atmosenv.2017.09.022.

Janjic, Z., Janjic, T., Vasic, R., 2011. A class of conservative fourth order advection schemes and impact of enhanced formal accuracy on extended range forecasts. Mon. Weather Rev. https://doi.org/10.1175/2010MWR3448.1.

Karydis, V.A., Kumar, P., Barahona, D., Sokolik, I.N., Nenes, A., 2011. On the effect of dust particles on global cloud condensation nuclei and cloud droplet numberm. J. Geophys. Res.-Atmos. 116 https://doi.org/10.1029/2011JD016283.

Kok, J.F., Ridley, D.A., Zhou, Q., Miller, R.L., Zhao, C., Heald, C.L., Ward, D.S., Albani, S., Haustein, K., 2017. Smaller desert dust cooling effect estimated from analysis of dust size and abundance. Nat. Geosci. 10 (4), 274–278. https://doi.org/10.1038/ngeo2912.

Lynch, P., Reid, J.S., Westphal, D.L., Zhang, J., Hogan, T.F., Hyer, E.J., Curtis, C.A., Hegg, D.A., Shi, Y., Campbell, J.R., Rubin, J.I., Sessions, W.R., Turk, F.J., Walker, A.L., 2016. An 11-year global gridded aerosol optical thickness reanalysis (v1.0) for atmospheric and climate sciences. Geosci. Model Dev. 9, 1489–1522.

Mahowald, N., Albani, S., Kok, J.F., Engelstaeder, S., Scanza, R., Ward, D.S., Flanner, M.G., 2014. The size distribution of desert dust aerosol and its impact on the Earth system. Aeolian Res. 15 (2014), 53–71. https://doi.org/10.1016/j.aeolia.2013.09.002.

Mahowald, N.M., Kloster, S., Engelstaedter, S., Moore, J.K., Mukhopadhyay, S., McConnell, J.R., Albani, S., Doney, S.C., Bhattacharya, A., Curran, M.A.J., Flanner, M.G., Hoffman, F.M., Lawrence, D.M., Lindsay, K., Mayewski, P.A., Neff, J., Rothenberg, D., Thomas, E., Thornton, P.E., Zender, C., 2010. S.: observed 20th century desert dust variability: impact on climate and biogeochemistry. Atmos. Chem. Phys. 10, 10875–10893. https://doi.org/10.5194/acp-10-10875-2010.

Mamouri, R.E., Ansmann, A., 2014. Fine and coarse dust separation with polarization lidar. Atmos. Meas. Tech. 7, 3717–3735. https://doi.org/10.5194/amt-7-3717-2014.

Mandija, F., Sicard, M., Comerón, A., Alados-Arboledas, L., Guerrero-Rascado, J.L., Barragan, R., Bravo-Aranda, J.A., Grandos-Muñoz, M.J., Lyamani, H., Muñoz Porcar, C., Rocadenbosch, F., Rodríguez, A., Valenzuela, A., García Vizcaíno, D., 2017. Origin and pathways of the mineral dust transport to two Spanish EARLINET sites: effect on the observed columnar and range-resolved dust optical properties. Atmos. Res. 187, 69–83. https://doi.org/10.1016/j.atmosres.2016.12.002.

Marinou, E., Tesche, M., Nenes, A., Ansmann, A., Schrod, J., Mamali, D., Tsekeri, A., Pikridas, M., Baars, H., Engelmann, R., Voudouri, K.-A., Solomos, S., Sciare, J., Groß, S., Ewald, F., Amiridis, V., 2019. Retrieval of ice-nucleating particle concentrations from lidar observations and comparison with UAV in situ measurements. Atmos. Chem. Phys. 19, 11315–11342. https://doi.org/10.5194/acp-19-11315-2019.

Mărmureanu, L., Marin, C.A., Andrei, S., Antonescu, B., Ene, D., Boldeanu, M., Vasilescu, J., Vițelaru, C., Cadar, O., Levei, E., 2019. Orange snow—a Saharan dust intrusion over Romania during winter conditions. Remote Sens. 11, 2466. https://doi.org/10.3390/rs11212466.

Mattis, I., D'Amico, G., Baars, H., Amodeo, A., Madonna, F., Iarlori, M., 2016. EARLINET Single Calculus Chain – technical – part 2: calculation of optical products. Atmos. Meas. Tech. 9, 3009–3029. https://doi.org/10.5194/amt-9-3009-2016.

McCoy, D.T., Bender, F.A.-M., Mohrmann, J.K.C., Hartmann, D.L., Wood, R., Grosvenor, D.P., 2017. The global aerosol-cloud first indirect effect estimated using MODIS, MERRA, and AeroCom. J. Geophys. Res. Atmos. 122, 1779–1796. https://doi.org/10.1002/2016JD026141.

Miffre, A., Cholleton, D., Mehri, T., Rairoux, P., 2019. Remote sensing observation of new particle formation events with a (UV, VIS) polarization Lidar. Remote Sens. 11 (15), 1761. https://doi.org/10.3390/rs11151761.

Navas-Guzmán, F., Martucci, G., Collaud Coen, M., Granados-Muñoz, M.J., Hervo, M., Sicard, M., Haefele, A., 2019. Characterization of aerosol hygroscopicity using Raman lidar measurements at the EARLINET station of Payerne. Atmos. Chem. Phys. 19, 11651–11668. https://doi.org/10.5194/acp-19-11651-2019.

Nicolae, D., et al., 2020. EARLINET/ACTRIS Analysis of Aerosol Profiles During the COVID-19 Lock-down and Relaxation Period. A Preliminary Study on Aerosol Properties in the Low and High Troposphere. https://www.earlinet.org/index.php?id=covid-19-reports.

Nisantzi, A., Mamouri, R.E., Ansmann, A., Schuster, G.L., Hadjikitsis, D.G., 2015. Middle East versus Saharan dust extinction-to-backscatter ratios. Atmos. Chem. Phys. 15, 7071–7084. https://doi.org/10.5194/acp-15-7071-2015.

Pérez, C., Nickovic, S., Pejanovic, G., Baldasano, J.M., Ozsoy, E., 2006. Interactive dust-radiation modeling: a step to improve weather forecasts. J. Geophys. Res. 11 https://doi.org/10.1029/2005JD006717.

Pérez, C., Haustein, K., Janjic, Z., Jorba, O., Huneeus, N., Baldasano, J.M., Black, T., Basart, S., Nickovic, S., Miller, R.L., Perlwitz, J.P., Schulz, M., Thomson, M., 2011. Atmospheric dust modeling from meso to global scales with the online NMMB/BSC-dust model – part 1: model description, annual simulations and evaluation. Atmos. Chem. Phys. 11, 13001–13027. https://doi.org/10.5194/acp-11-13001-2011.

Pisso, I., Sollum, E., Grythe, H., Kristiansen, N.I., Cassiani, M., Eckhardt, S., Arnold, D., Morton, D., Thompson, R.L., Groot Zwaaftink, C.D., Evangeliou, N., Sodemann, H., Haimberger, L., Henne, S., Brunner, D., Burkhart, J.F., Fouilloux, A., Brioude, J., Philipp, A., Seibert, P., Stohl, A., 2019. The Lagrangian particle dispersion model

FLEXPART version 10.4. Geosci. Model Dev. 12, 4955–4997. https://doi.org/10.5194/gmd-12-4955-2019.

Radenz, M., Seifert, P., Baars, H., Floutsi, A.A., Yin, Z., Bühl, J., 2021. Automated time–height-resolved air mass source attribution for profiling remote sensing applications. Atmos. Chem. Phys. 21, 3015–3033. https://doi.org/10.5194/acp-21-3015-2021.

Rother, T., Kahnert, M., 2009. Electromagnetic Wave Scattering on Nonspherical Particles. In: Springer Series in Optical Sciences, 145. SSOS. https://doi.org/10.1007/978-3-642-00704-0.

Ryder, C.L., Highwood, E.J., Walser, A., Seibert, P., Philipp, A., Weinzierl, B., 2019. Coarse and giant particles are ubiquitous in Saharan dust export regions and are radiatively significant over the Sahara. Atmos. Chem. Phys. 19, 15353–15376. https://doi.org/10.5194/acp-19-15353-2019.

Samaras, S., 2016. Microphysical Retrieval of Non-spherical Aerosol Particles Using Regularized Inversion of Multi-wavelength Lidar Data. PhD Thesis. University of Potsdam, Germany. Institute of Mathematics. http://nbn-resolving.de/urn:nbn:de:kobv:517-opus4-396528.

Samaras, S., Böckmann, C., Ritter, C., 2022. Modeling a spheroidal particle ensemble and inversion by generalized Runge–Kutta regularizers from limited data. AppliedMath 2, 547–573. https://doi.org/10.3390/appliedmath2040032.

Seibert, P., Frank, A., 2004. Source–receptor matrix calculation with a Lagrangian particle dispersion model in backward mode. Atmos. Chem. Phys. 4, 51–63. https://doi.org/10.5194/acp-4-51-2004.

Seinfeld, J.H., Pandis, S.N., 2006. Atmospheric Chemistry and Physics: From Air Pollution to Climate Change, 2nd edition. John Wiley & Sons, New York.

Seinfeld, J.H., Bretherton, C., Carslaw, K.S., Coe, H., DeMott, P.J., Dunlea, E.J., Feingold, G., Ghan, S., Guenther, A.B., Kahn, R., Kraucunas, I., Kreidenweis, S.M., Molina, M.J., Nenes, A., Penner, J.E., Prather, K.A., Ramanathan, V., Ramaswamy, V., Rasch, P.J., Ravishankara, A.R., Rosenfeld, D., Stephens, G., Wood, R., 2016. Improving our fundamental understanding of the role of aerosol–cloud interactions in the climate system. Proc. Natl. Acad. Sci. U. S. A. 113, 5781–5790. https://doi.org/10.1073/pnas.1514043113.

Shin, S.-K., Tesche, M., Kim, K., Kezoudi, M., Tatarov, B., Müller, D., Noh, Y., 2018. On the spectral depolarisation and lidar ratio of mineral dust provided in the AERONET version 3 inversion product. Atmos. Chem. Phys. 18, 12735–12746. https://doi.org/10.5194/acp-18-12735-2018.

Soupiona, O., Samaras, S., Ortiz-Amezcua, P., Böckmann, C., Papayannis, A., Moreira, G.A., Benavent-Oltra, J.A., Guerrero-Rascado, J.L., Bedoya-Velásquez, A.E., Olmo, F.J., Román, R., Kokkalis, P., Mylonaki, M., Alados-Arboledas, L., Papanikolaou, C.A., Foskinis, R., 2019. Retrieval of optical and microphysical properties of transported Saharan dust over Athens and Granada based on multi-wavelength Raman lidar measurements: study of the mixing processes. Atmos. Environ. 214, 116824.

Soupiona, O., Papayannis, A., Kokkalis, P., Foskinis, R., Sánchez Hernández, G., Ortiz-Amezcua, P., Mylonaki, M., Papanikolaou, C.-A., Papagiannopoulos, N., Samaras, S., Groß, S., Mamouri, R.-E., Alados-Arboledas, L., Amodeo, A., Psiloglou, B., 2020. EARLINET observations of Saharan dust intrusions over the northern Mediterranean region (2014–2017): properties and impact on radiative forcing. Atmos. Chem. Phys. 20, 15147–15166. https://doi.org/10.5194/acp-20-15147-2020.

Stachlewska, I.S., Costa-Surós, M., Althausen, D., 2017. Raman lidar water vapour profiling over Warsaw, Poland. Atmos. Res. 194, 258–267. https://doi.org/10.1016/j.atmosres.2017.05.004.

Stachlewska, I.S., Samson, M., Zawadzka, O., Harenda, K.M., Janicka, L., Poczta, P., Szczepanik, D., Heese, B., Wang, D., Borek, K., Tetoni, E., Proestakis, E., Siomos, N., Nemuc, A., Chojnicki, B.H., Markowicz, K.M., Pietruczuk, A., Szkop, A., Althausen, D., Stebel, K., Schuettemeyer, D., Zehner, C., 2018. Modification of local urban aerosol properties by long-range transport of biomass burning aerosol. Remote Sens. 10 (3), 412 https://doi.org/10.3390/rs10030412.

Stein, A.F., Draxler, R.R., Rolph, G.D., Stunder, B.J.B., Cohen, M.D., Ngan, F., 2015. NOAA's HYSPLIT atmospheric transport and dispersion modeling system. Bull. Am. Meteorol. Soc. 96, 2059–2077. https://doi.org/10.1175/BAMS-D-14-00110.1.

Stohl, A., Forster, C., Frank, A., Seibert, P., Wotawa, G., 2005. Technical note: the Lagrangian particle dispersion model FLEXPART version 6.2. Atmos. Chem. Phys. 5, 2461–2474. https://doi.org/10.5194/acp-5-2461-2005.

Szczepanik, D., Tetoni, E., Wang, D., Stachlewska, I.S., 2020. Lidar based separation of polluted dust observed over Warsaw (case study on 09 August 2013). EPJ Web Conf. 237 (02018), 2020. https://doi.org/10.1051/epjconf/202023702018.

Szczepanik, D.M., Stachlewska, I.S., Tetoni, E., Althausen, D., 2021. Properties of Saharan dust versus local urban dust—a case study. Earth Space Sci. 8 (12), e2021EA001816 https://doi.org/10.1029/2021EA001816.

Szczepanik, D.M., Ortiz-Amezcua, P., Heese, B., D'Amico, G., Stachlewska, I.S., 2022. First ever observations of mineral dust in wintertime over Warsaw, Poland. Remote Sens. 14 (15), 3788.

Talianu, C., Seibert, P., 2019. Analysis of sulfate aerosols over Austria: a case study. Atmos. Chem. Phys. 19, 6235–6250. https://doi.org/10.5194/acp-19-6235-2019.

Tsarpalis, K., Papadopoulos, A., Mihalopoulos, N., Spyrou, C., Michaelides, S., Katsafados, P., 2018. The implementation of a mineral dust wet deposition scheme in the GOCART-AFWA module of the WRF model. Remote Sens. 10, 1595. https://doi.org/10.3390/rs10101595.

Veselovskii, I., Goloub, P., Podvin, T., Bovchaliuk, V., Derimian, Y., Augustin, P., Fourmentin, M., Tanre, D., Korenskiy, M., Whiteman, D.N., Diallo, A., Ndiaye, T., Kolgotin, A., Dubovik, O., 2016. Retrieval of optical and physical properties of African dust from multiwavelength Raman lidar measurements during the SHADOW campaign in Senegal. Atmos. Chem. Phys. 16, 7013–7028. https://doi.org/10.5194/acp-16-7013-2016.

Wang, D., Szczepanik, D., Stachlewska, I.S., 2019. Interrelations between surface, boundary layer, and columnar aerosol properties derived in summer and early autumn over a continental urban site in Warsaw, Poland. Atmos. Chem. Phys. 19, 13097–13128. https://doi.org/10.5194/acp-19-13097-2019.

Wang, D., Stachlewska, I.S., Delanoë, J., Ene, D., Song, X., Schüttemeyer, D., 2020. Spatio-temporal discrimination of molecular, aerosol and cloud scattering and polarization using a combination of a Raman lidar, Doppler cloud radar and microwave radiometer. Opt. Express 28, 20117–20134.

Weger, M., Heinold, B., Engler, C., Schumann, U., Seifert, A., Fößig, R., Voigt, C., Baars, H., Blahak, U., Borrmann, S., Hoose, C., Kaufmann, S., Krämer, M., Seifert, P., Senf, F., Schneider, J., Tegen, I., 2018. The impact of mineral dust on cloud formation during the Saharan dust event in April 2014 over Europe. Atmos. Chem. Phys. 18, 17545–17572. https://doi.org/10.5194/acp-18-17545-2018.

Woś, A., 2010. Klimat Polski w Drugiej Połowie XX wieku. Wydawnictwo Naukowe UAM, Poznań.

Wu, D., Liu, J., Wang, T., Niu, X., Chen, Z., Wang, D., Zhang, X., Ji, M., Wang, X., Pu, W., 2020. Applying a dust index over North China and evaluating the contribution of potential factors to its distribution. Atmos. Res. 254, 105515 https://doi.org/10.1016/j.atmosres.2021.105515.

Zhang, J., Campbell, J.R., Hyer, E.J., Reid, J.S., Westphal, D.L., Johnson, R.S., 2014. Evaluating the impact of multisensor data assimilation on a global aerosol particle transport model. J. Geophys. Res. Atmos. 119, 4674–4689. https://doi.org/10.1002/2013JD020975.

Żmudzka, E., 2016. Zmienność czasowa i zróżnicowanie przestrzenne podstawowych elementów klimatu w wybranych punktach pomiarowych na terenie Warszawy (1981–2014). Wydział Geografii i Studiów Regionalnych Uniwersytetu Warszawskiego, Warsaw.

Żmudzka, E., Kulesza, K., Lenartowicz, M., Leziak, K., Magnuszewski, A., 2019. Assessment of modern hydro-meteorological hazards in a big cit – identification for Warsaw. Meteorol. Appl. 26, 500–510. https://doi.org/10.1002/met.1779.